Biorheology 52 (2015) 183–210
DOI 10.3233/BIR-14033
IOS Press

Hemodynamics in stenotic vessels of small diameter under steady state conditions: Effect of viscoelasticity and migration of red blood cells

Yannis Dimakopoulos [a,b,*], George Kelesidis [a], Sophia Tsouka [a], Georgios C. Georgiou [b] and John Tsamopoulos [a]

[a] *Laboratory of Fluid Mechanics and Rheology, Department of Chemical Engineering, University of Patras, Patras, Greece*

[b] *Department of Mathematics and Statistics, University of Cyprus, Nicosia, Cyprus*

Received 7 October 2014
Accepted 14 July 2015

Abstract.
BACKGROUND: In microcirculation, the non-Newtonian behavior of blood and the complexity of the microvessel network are responsible for the high flow resistance and the large reduction of the blood pressure. Red blood cell aggregation along with inward radial migration are two significant mechanisms determining the former. Yet, their impact on hemodynamics in non-straight vessels is not well understood.
OBJECTIVE: In this study, the steady state blood flow in stenotic rigid vessels is examined, employing a sophisticated non-homogeneous constitutive law. The effect of red blood cells migration on the hydrodynamics is quantified and the constitutive model's accuracy is evaluated.
METHODS: A numerical algorithm based on the two-dimensional mixed finite element method and the EVSS/SUPG technique for a stable discretization of the mass and momentum conservation equations in addition to the constitutive model is employed.
RESULTS: The numerical simulations show that a cell-depleted layer develops along the vessel wall with an almost constant thickness for slow flow conditions. This causes the reduction of the drag force and the increase of the pressure gradient as the constriction ratio decreases.
CONCLUSIONS: Viscoelastic effects in blood flow were found to be responsible for steeper decreases of tube and discharge hematocrits as decreasing function of constriction ratio.

Keywords: RBC migration, shear-induced migration, Fahraeus–Lindqvist effect, blood viscoelasticity, stenotic microvessels, cell-depleted layer

1. Introduction

Microvessels have a very significant role for the hemostasis of organs and tissues. Blood flows through them and delivers oxygen and nutrients to the organs, where they are exchanged with carbon oxides

*Address for correspondence: Yannis Dimakopoulos, Dr., Laboratory of Fluid Mechanics and Rheology, Department of Chemical Engineering, University of Patras, Patras, Greece. E-mail: dimako@chemeng.upatras.gr.

and metabolic wastes. In all cases the chemical carriers are the red blood cells (RBCs). In terms of hemodynamics, about 80% of the total pressure drop of the circulation takes place in microvessels (Popel and Johnson [1], Lipowsky [2]), because of their small diameter ($\leqslant$300 μm) which is comparable to that of RBCs ($\leqslant$8 μm) (Freund [3]). This has many implications on the flow field: the velocity profiles are not parabolic, the apparent viscosity is not constant and depends on the vessel diameter, the haematocrit is also dependent on the vessel diameter, phase separation occurs at bifurcations and a cell-free layer is formed along the wall (Sharan and Popel [4]).

Blood consists of a concentrated suspension of blood cells in plasma. Of the formed elements, the white blood cells together with the platelets occupy less than one percent of the volume of blood, while the RBCs form the dominant matter of blood, occupying about 45% and 40% of the volume for men and women, respectively (Baskurt [5], Chien [6], Chien et al. [7]). Thus, the rheological properties of blood are primarily governed by the concentration of RBCs and their behavior at different shear rates. As the blood flows through microtubes, non-Newtonian effects, such as shear-thinning and viscoelasticity, become more important. At low shear rates ($\dot{\gamma} < 10\ \mathrm{s}^{-1}$), the RBCs tend to aggregate and form column-like structures called rouleaux, which increase the blood viscosity (Meiselman [8]). At even lower shear rates ($\dot{\gamma} < 1\ \mathrm{s}^{-1}$), these rouleaux develop branches and eventually three-dimensional complex networks, inducing an additional increase of the viscosity. On the contrary, increasing the shear rate leads to the breaking up of rouleaux, alignment of the RBCs with the rouleaux and finally deformation of the RBCs and reduction of the viscosity. This tendency of RBCs to agglomerate and disaggregate in addition to their deformability is responsible for the shear thinning character of blood. On the other hand, the deformability and orientation of rouleaux and individual RBCs provides a means of storing energy during flow, leading to the viscoelastic behavior of blood. Thurston [9] investigated *in vitro* viscoelastic properties of blood in the linear viscoelastic regime and measured a significant elastic component in oscillatory blood flow. He also measured the shear-rate dependence of the viscoelastic properties of blood at a given frequency (Thurston [10]). Evans and Hochmuth [11] have found that the RBC membrane exhibits stress relaxation. From these measurements, the non-linear viscoelastic properties of blood are evident.

Several constitutive models for the stresses of the model have been developed in order to present the viscoelastic, shear-thinning character as well as the non-homogeneous phenomena of blood flow (Apostolidis and Beris [12]). Quemada [13] derived a generalized Maxwell constitutive model by assuming that aggregation and disaggregation are simple relaxation processes and developed a relation between the number fraction of red blood cells in aggregates and the mean relaxation times of aggregation and disaggregation. Williams et al. [14] also derived a Maxwell model, based on quite a few restrictions, including that flow conditions are near equilibrium and that the rouleaux are "long". Vlastos et al. [15] examined viscoelastic effects and proposed a Carreau model for the description of blood shear-thinning (see also Dimakopoulos et al. [16]). Anand et al. [17] proposed a viscoelastic model that is based on the thermodynamic framework developed by Rajagopal and Srinivasa [18]. The model accounts for the dependence of the relaxation times on the shear rate and is in good agreement with experimental data in steady Poiseuille flow and oscillatory flow (Bodnar and Sequeira [19]). Chakraborty et al. [20] evaluated three viscoelastic models for the simulation of blood flow in a two-dimensional collapsible channel. This was one of the first studies in fluid-structure interaction with a viscoelastic assumption for the blood rheology.

Quite recently two constitutive models were proposed by Owens and collaborators (Moyers-Gonzalez et al. [21], Owens [22]) that can be used even in microflows: flows in arterioles, venules or in general vessels of diameter larger than 50 μm, which is the lower limit for a continuum approximation. Owens [22] used a macroscopic continuum model which rests on sound microscopic-level foundations. The

aggregation and disaggregation of RBCs are modeled using ideas drawn from the temporary polymer network theory. The basic microstructural unit is represented as an elastic dumbbell which is able to attach to and detach itself from larger aggregates. He showed that predictions of shear stress hysteresis loops in triangular hysteresis experiments in a Couette rheometer were in close agreement with the experimental data of Bureau et al. [23] and resulted from a complex interplay of shear-thinning, viscoelastic and thixotropic effects. Fang and Owens [24] used it to investigate the steady, oscillatory and pulsatile flow of blood in a tube of radius 0.43 mm. Elastic effects of blood were most pronounced at low flow rates and low flow rate amplitudes, and the agreement with data from (Thurston [10,25]) was satisfactory. Subsequently, Iolov et al. [26] simulated steady and pulsatile flow in two and three dimensions for straight and aneurytic geometries of vessels. Although the flow parameters were such that the effect of elasticity was small, noticeable differences were reported between the Newtonian and non-Newtonian flows, especially in the pulsating case.

Moyers-Gonzalez et al. [21] extended the constitutive model of Owens to describe non-homogeneous flows of human blood. In order to account for the Fahraeus [27] and Fahraeus–Lindqvist [28] effects, they derived the model starting with the basic equations in a solution of non-interacting dumbbells for the number density and polymeric stress and making standard arguments of the polymer kinetic theory, already used by Beris and Mavrantzas [29], Bhave et al. [30], Cook and Rossi [31] and Rossi et al. [32]. The numerical results for one-dimensional steady axisymmetric flow in a uniform pipe were found to be very close to those obtained using the empirical expression of Pries et al. [33] for the apparent viscosity. Although the representation of RBC aggregates as elastic dumbbells neglects the motion of individual RBCs, it can sufficiently describe the macroscopic blood flow, as good agreement with experiments and empirical relationships was obtained by Owens [22] and Moyers-Gonzalez et al. [21]. A Lagrangian approach (direct numerical simulation) could capture microscopic phenomena, such as the rotation and sliding of RBCs upon the aggregate stretching, but this would require a much larger computational cost in terms of time and memory to simulate systems with realistic RBC number densities. Moreover, there is a number of significant open issues on the accurate constitutive modeling of a RBC membrane and the electrochemical path for their intercellular interaction. In all cases a statistical average of stresses and RBC population is finally provided. Thus, an Eulerian framework employing the Moyers-Gonzalez et al. [21] model, which is based on the use of averaged constitutive and population balances could facilitate the simulation of blood flow in stenotic vessels and provide a better understanding of non-homogeneous phenomena, i.e. the Fahraeus [27] and Fahraeus–Lindqvist effects [28], that are present.

The Fahraeus [27] and Fahraeus–Lindqvist [28] effects are very significant, and appear only in microtubes. The decrease of the average concentration of red blood cells, known as dynamic haematocrit, as the vessel's diameter decreases is known as the Fahraeus effect. The mathematical approach of Sutera et al. [34] showed that because of the migration of RBCs from the vessel walls towards the axis of symmetry, the dynamic haematocrit in the vessel (tube haematocrit) must be less than that of the blood discharged from the end of the tube (discharge haematocrit). Pries et al. [33] provided an empirical parametric expression in order to calculate the dynamic haematocrit through the feed/discharge haematocrit. The Fahraeus–Lindqvist effect may be considered as a consequence of the Fahraeus effect, as the migration of RBCs from the wall to the vessel's center leads to the development of a cell-depleted layer with a lower viscosity on the wall, serving as a lubricating layer. Although the thickness of the cell-depleted layer depends on the flow rate and the diameter, it seems to do so weakly and the layer thickness remains more or less in the range of 2–4 μm (Caro et al. [35]). Therefore, the relative volume of the slippage layer increases as the tube diameter decreases. This, combined with the Fahraeus effect, results in a decrease in the apparent viscosity.

The current work firstly aims at developing a stable numerical framework for the simulation of the inhomogeneous blood model (Moyers-Gonzalez et al. [21]) in a stenosed microvessel. In addition, local effects and their characteristics such as the cell-depleted layer are systematically studied. In the second and third sections, we present the mathematical modeling of the problem and its numerical solution, respectively. Finally, in the last two sections we evaluate its efficiency to describe the non-homogeneous phenomena, discuss the results and draw our conclusions.

2. Problem formulation

2.1. Definition of the physical problem

We consider the steady, axisymmetric flow of blood through a stenotic micro-vessel with sinusoidal axial variation (Fig. 1) of its rigid boundary. To reduce the effect of boundary entrance and exit conditions, we impose periodicity in the flow field. The dimensional local height of the undulating tube along the z-axis varies according to the following formula:

$$\tilde{R}(\tilde{z}) = \begin{cases} \tilde{R}_{\max}, & 0 \leqslant \tilde{z} \leqslant \tilde{L}_{\mathrm{e}}, \\ \tilde{h} + \tilde{a}\cos\big(2\pi(\tilde{z} - \tilde{L}_{\mathrm{e}})/(\tilde{L} - 2\tilde{L}_{\mathrm{e}})\big), & \tilde{L}_{\mathrm{e}} \leqslant \tilde{z} \leqslant \tilde{L} - \tilde{L}_{\mathrm{e}}, \\ \tilde{R}_{\max}, & \tilde{L} - \tilde{L}_{\mathrm{e}} \leqslant \tilde{z} \leqslant \tilde{L}. \end{cases} \tag{1}$$

The amplitude of the undulation in the geometry is denoted as $\tilde{a} = \frac{\tilde{R}_{\max} - \tilde{R}_{\min}}{2}$, while the average radius of an equivalent straight vessel of length $\tilde{L} - 2\tilde{L}_{\mathrm{e}}$ is equal to $\tilde{h} = \frac{\tilde{R}_{\max} + \tilde{R}_{\min}}{2}$, where $\tilde{R}_{\min}$ and $\tilde{R}_{\max}$ are the minimum and maximum radii of the undulation in relation to the axis of symmetry, respectively. In addition, the total length of the vessel is equal to $\tilde{L}$, the lengths of both the entrance and exit section of the vessel are equal to $\tilde{L}_{\mathrm{e}}$. The notation "~" will indicate dimensional quantities.

Here, blood is considered to be a viscoelastic solution with a varying relaxation time $\tilde{\mu}$, incompressible with constant density $\tilde{\rho}$. The plasma viscosity is constant equal to $\tilde{\eta}_{\mathrm{p}}$, and $\tilde{\eta}_{\mathrm{C}}$ is RBC contributions to the viscosity of the blood. In particular, it is assumed to be a three-phase system made of plasma, individual RBCs and RBC aggregates in the form of rouleaux. According to the definition of Iolov et al. [26], $\tilde{\eta}_{\mathrm{c}}$ is given by the non-linear expression: $\tilde{\eta}_{\mathrm{c}} = \tilde{N}(k_{\mathrm{B}}\tilde{T} + \kappa)\tilde{\mu}(\tilde{\dot{\gamma}}, \tilde{N}, \tilde{M})$, where $\tilde{N}$ is the red blood cell number density, k_{B} is the Boltzmann constant, $\tilde{T}$ is the absolute temperature, κ is a constant with units of energy that accounts for the impact of red blood cell interactions on viscosity and $\tilde{\mu}$ is the relaxation time of the rouleaux of the RBCs that is a non-linear function of the shear-rate, $\tilde{\dot{\gamma}}$, and the average rouleau size, $\tilde{n}$, which in turn is a function of the red blood cell and rouleau number density

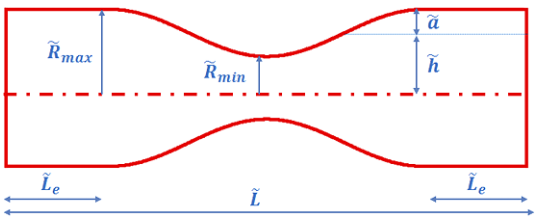

Fig. 1. Schematic of a stenotic axisymmetric vessel. (Colors are visible in the online version of the article; http://dx.doi.org/10.3233/BIR-14033.)

(see the Appendix). Concerning the effective translational diffusivity $\tilde{D}_{\rm tr}$ of the migrating RBCs, it is an assumption required by the original model of Moyers-Gonzalez et al. [21] to consider it a constant accounting only for the Brownian collisions of a dumbbell with its neighbors, while neglecting the strong dependence on hematocrit and local shear rate (e.g. Zydney and Colton [36], Bishop et al. [37], Acrivos [38]).

To perform a systematic study in the parameter space, we have to bring the governing equations and geometric characteristics into a dimensionless form. To this end, we define the following set of characteristic quantities: We scale all lengths with the maximum radius of the tube $\tilde{l}^* = \tilde{R}_{\rm max}$. As a characteristic scale for the velocity we use the mean velocity $\tilde{u}^* = \langle \underline{\tilde{u}} \rangle = \tilde{u}_{\rm m} = \frac{\int\int \tilde{u}_{\tilde{z}} \tilde{r}\, {\rm d}\tilde{r}}{\int\int r\, {\rm d}\tilde{r}}$. For the characteristic value of viscosity we consider the following: At infinite shear-rates the RBC density reduces to the average RBC number density $\langle \tilde{N} \rangle = \frac{\int\int \tilde{N} \tilde{r}\, {\rm d}\tilde{r}\, {\rm d}\tilde{z}}{\int\int \tilde{r}\, {\rm d}\tilde{r}\, {\rm d}\tilde{z}}$, which is a function of the vessel radius $\tilde{R}$, while the relaxation time reduces to the single RBC relaxation time $\tilde{\lambda}$, yielding the formula for the infinite-shear RBC viscosity $\tilde{\eta}_\infty(\tilde{R}) = \langle \tilde{N} \rangle (k_{\rm B}\tilde{T} + \kappa)\tilde{\lambda}$. Considering that for the case of infinite radius, $\langle \tilde{N} \rangle$ reaches the asymptotic value of homogeneous flow $\langle \tilde{N}_{\rm Hom} \rangle$, reducing the infinite-shear RBC viscosity to $\tilde{\eta}_\infty(\infty) = \langle \tilde{N}_{\rm Hom} \rangle (k_{\rm B}\tilde{T} + \kappa)\tilde{\lambda}$, which is selected as the characteristic value for the RBC viscosity $\tilde{\eta}^*_{\rm C}$. The characteristic value of the total blood viscosity $\tilde{\eta}^*_{\rm t}$ is obtained as the sum of $\tilde{\eta}^*_{\rm C}$ and the plasma viscosity $\tilde{\eta}_{\rm p}$, yielding $\tilde{\eta}^*_{\rm t} = \langle \tilde{N}_{\rm Hom} \rangle (k_{\rm B}\tilde{T} + \kappa)\tilde{\lambda} + \tilde{\eta}_{\rm p}$. The number density of RBCs ($\tilde{N}$) and rouleaux ($\tilde{M}$) is non-dimensionalized with the asymptotic average value of RBC number density in a homogeneous flow, $\tilde{N}^* = \langle \tilde{N}_{\rm Hom} \rangle$. Finally, all stress tensors and pressure are scaled with a viscous scale $\tilde{\tau}^* = \tilde{P}^* = \frac{\tilde{\eta}^*_{\rm t} \tilde{u}_{\rm m}}{\tilde{R}_{\rm max}}$, the rate of strain tensor with $\tilde{\dot{\gamma}}^* = \frac{\tilde{u}_{\rm m}}{\tilde{R}_{\rm max}}$, and time with $\tilde{t}^* = \frac{\tilde{l}^*}{\tilde{u}^*} = \frac{\tilde{R}_{\rm max}}{\tilde{u}_{\rm m}}$. Typical values of the resulting characteristic numbers and of the main physical properties of the problem are given in Table 1.

The dimensionless characteristic numbers that arise in the governing equations are the following:

- The Reynolds number,

$$Re = \frac{\tilde{\rho} \tilde{u}_{\rm m} \tilde{R}_{\rm max}}{\tilde{\eta}_{\rm t}} \tag{2}$$

  which is the ratio of inertial to viscous forces.

Table 1

Material and flow parameters for blood flow in rigid tubes, as obtained from Table 1 and Appendix of Moyer-Gonzalez et al. [8,21]

Parameter	Symbol	Assigned value	Units
Plasma viscosity	$\tilde{\eta}_{\rm p}$	0.001	Pa · s
Infinite-shear-rate viscosity	$\tilde{\eta}_\infty$	0.00234	Pa · s
Zero-shear-rate viscosity	$\tilde{\eta}_0$	0.0326	Pa · s
Critical shear rate	$\tilde{\dot{\gamma}}_{\rm cr}$	5.78	s^{-1}
Maximum shear rate	$\tilde{\dot{\gamma}}_{\rm max}$	900	s^{-1}
Cross model power-law exponent	M	2.1238	–
Cross model parameter	$\tilde{\varepsilon}$	0.7014	s^m
Cross model parameter	$\tilde{\theta}$	$\tilde{\eta}_\infty \tilde{\beta}_{\rm c}/\tilde{\eta}_0$	s^m
Maxwell single cell relaxation time	$\tilde{\lambda}$	0.005	s
Translational diffusivity	$\tilde{D}_{\rm tr}$	$2 \cdot 10^{-10}$	m^2/s
Average number density of RBCs in homogeneous flow	$\tilde{N}_{\rm m}$	$5 \cdot 10^{15}$	m^{-3}

- The Deborah number,

$$De = \frac{\tilde{\lambda}\tilde{u}_{\mathrm{m}}}{\tilde{R}_{\max}} \tag{3}$$

  which is the ratio of the fluid relaxation time to a characteristic time for the macroscopic flow.
- The Peclet number,

$$Pe = \frac{\tilde{u}_{\mathrm{m}}\tilde{R}_{\max}}{\tilde{D}_{\mathrm{tr}}} \tag{4}$$

  which is the ratio of the convective flux to the diffusive flux of RBCs and their rouleaux.
- The ratio of plasma to total viscosity,

$$\beta = \frac{\tilde{\eta}_{\mathrm{p}}}{\tilde{\eta}_{\mathrm{t}}} \tag{5}$$

  which is related to the haematocrit.

We also report the dimensionless form of the vessel surface equation, which reads:

$$R(z) = \begin{cases} 1, & 0 \leqslant z \leqslant L_{\mathrm{e}}, \\ \dfrac{1}{2}(1+c_{\mathrm{r}}) + \dfrac{1}{2}(1-c_{\mathrm{r}})\cos\big(2\pi(z-L_{\mathrm{e}})/(L-2L_{\mathrm{e}})\big), & L_{\mathrm{e}} \leqslant z \leqslant L-L_{\mathrm{e}}, \\ 1, & L-L_{\mathrm{e}} \leqslant z \leqslant L, \end{cases} \tag{6}$$

where $c_{\mathrm{r}} = \tilde{R}_{\min}/\tilde{R}_{\max}$ is the constriction ratio, L is dimensionless total length of the vessel and $L_{\mathrm{e}} = \tilde{L}_{\mathrm{e}}/\tilde{R}_{\max}$ is dimensionless length of the entrance and exit section of the vessel.

2.2. Governing equations

Our analysis begins with the extended microstructure model for human blood flow derived by Moyers-Gonzalez et al. [21]. The model accounts for both individual RBCs and aggregates of RBCs in terms of concentration and stresses. Each rouleaux of RBCs is composed of k RBCs and represented as a Hookean elastic dumbbell. Denoting the dimensionless number density of k-mers as N_k, we define the quantities:

- The scaled number density of all RBCs, either isolated or after forming rouleaux:

$$N = \sum_{k=1}^{\infty} kN_k. \tag{7}$$

- The scaled number density of rouleaux:

$$M = \sum_{k=1}^{\infty} N_k. \tag{8}$$

- The average rouleaux size:

$$n = n(N, M) = \frac{N}{M}. \tag{9}$$

A key factor in explicitly solving the transfer problem of RBCs was the diffusion and momentum coupling through a generalized definition of the flux vector of each species: $\underline{J}$ and $\underline{I}$ for individual RBCs and rouleaux, respectively. These are given by the following relations:

$$\underline{J} = -\frac{1}{Pe}\left(\underline{\nabla} N - \frac{De}{1-\beta}\underline{\nabla}\cdot\underline{\underline{\tau}}\right), \tag{10}$$

$$\underline{I} = -\frac{1}{Pe}\left(\underline{\nabla} M - \frac{De}{1-\beta}\underline{\nabla}\cdot\underline{\underline{\sigma}}\right), \tag{11}$$

where $\underline{\underline{\tau}}$ and $\underline{\underline{\sigma}}$ are the elastic stress tensors for the individual RBCs and Rouleaux, respectively. $\underline{\nabla} N$ and $\underline{\nabla} M$ accounts for the Brownian motion of both individual RBCs and rouleaux, while $\underline{\nabla}\cdot\underline{\underline{\tau}}$ and $\underline{\nabla}\cdot\underline{\underline{\sigma}}$ represent the stress-gradient induced transfer of both species (Beris and Mavrantzas [29]). It should be mentioned that the model does not include hydrodynamic and wall effects, which are important when the flow geometry is confined or the hematocrit is physiological (Pranay et al. [39], Ma and Graham [40]).

The population balances for the number density of the RBCs (N) and the aggregates (M) are:

$$\frac{DN}{Dt} = -\underline{\nabla}\cdot\underline{J} \equiv \frac{1}{Pe}\underline{\nabla}^2 N - \frac{1}{(1-\beta)}\frac{De}{Pe}\underline{\underline{\nabla\nabla}} : \underline{\underline{\tau}}, \tag{12}$$

$$\frac{DM}{Dt} = -\underline{\nabla}\cdot\underline{I} \equiv \frac{1}{Pe}\underline{\nabla}^2 M - \frac{1}{(1-\beta)}\frac{De}{Pe}\underline{\underline{\nabla\nabla}} : \underline{\underline{\sigma}} - 0.5\alpha(\dot{\gamma})\frac{N}{n}M + 0.5b(\dot{\gamma})(N-M), \tag{13}$$

where $a(\dot{\gamma})$ and $b(\dot{\gamma})$ are the aggregation and the fragmentation rates of rouleaux (defined in Appendix A.2), and $\dot{\gamma}$ is the second invariant of the rate of strain tensor.

In Eqs (12) and (13), the fluxes are caused either by species diffusion (1st term in the right-hand side) or stress-induced migration (2nd term) and in the case of rouleaux by the aggregation–disaggregation kinetics (3rd and 4th terms). The ratio $\frac{De}{Pe}$ is equal to the ratio of the diffusive length scale over the characteristic length scale of the macroscopic flow ($\frac{\tilde{\lambda}\tilde{D}_{\rm tr}}{\tilde{R}^2_{\rm max}}$). The diffusive length is defined here as the distance $(\tilde{\lambda}\tilde{D}_{\rm tr})^{1/2}$ that a RBC traverses within a time equal to the corresponding relaxation time of the RBC membrane. This is a very important parameter, since, as we will discuss later on, it determines the width of the layer in the flow domain (typically near the vessel walls) which is depleted of RBCs.

Moreover, the velocity field ($\underline{u}$) results from the momentum and mass balances:

$$Re\frac{D\underline{u}}{Dt} = -\underline{\nabla} P_{\rm per} - K^2\underline{e}_z + \underline{\nabla}\cdot\underline{\underline{\tau}} + \beta\nabla^2\underline{u}, \tag{14}$$

$$\underline{\nabla}\cdot\underline{u} = 0, \tag{15}$$

where $P_{\rm per} = P - K^2 z$ denotes the periodic part of the pressure, $K^2 = \frac{|\Delta P|}{L}$ is the constant pressure gradient in a vessel, and the material derivative is defined as:

$$\frac{D\circ}{Dt} = \frac{\partial\circ}{\partial t} + \underline{u}\cdot\underline{\nabla}\circ. \tag{16}$$

Originally, the idea of coupling the diffusion and the momentum was introduced by Beris and Mavrantzas [29] and Bhave et al. [30] in the case of a dilute polymer solution under shear flow conditions in order to study the migration of polymer due to a tensorial stress field.

As far as the constitutive modeling for both individual and aggregated RBCs is concerned, we use the modified Oldroyd-B constitutive law in which we have included stress-gradient migration phenomena. They read

$$\underline{\underline{\tau}} + De\mu(\dot{\gamma}, N, M)\underline{\underline{\tau}}_{(1)} - \frac{De}{Pe}\mu(\dot{\gamma}, N, M)\left(\nabla^2\underline{\underline{\tau}} + (\underline{\underline{\nabla\nabla}} : \underline{\underline{\tau}})\underline{\underline{I}}\right) = (1-\beta)\mu(\dot{\gamma}, N, M)N\underline{\underline{\dot{\gamma}}}, \tag{17}$$

$$\underline{\underline{\sigma}} + De\mu(\dot{\gamma}, N, M)\underline{\underline{\sigma}}_{(1)} - \frac{De}{Pe}\mu(\dot{\gamma}, N, M)\left(\nabla^2\underline{\underline{\sigma}} + (\underline{\underline{\nabla\nabla}} : \underline{\underline{\sigma}})\underline{\underline{I}}\right) = (1-\beta)\mu(\dot{\gamma}, N, M)M\underline{\underline{\dot{\gamma}}}, \tag{18}$$

where $\mu(\dot{\gamma}, N, M)$ is the relaxation-time function, $\underline{\underline{\dot{\gamma}}}$ is the rate-of-strain tensor defined as:

$$\underline{\underline{\dot{\gamma}}} = \frac{1}{2}\left[(\underline{\nabla}\,\underline{u})^{\mathrm{T}} + \underline{\nabla}\,\underline{u}\right] \tag{19}$$

and where $\underline{\underline{I}}$ denotes the unit tensor and $\langle\,\rangle_{(1)}$ the upper convected time derivative defined as:

$$\langle\,\rangle_{(1)} = \frac{D\langle\,\rangle}{D\tilde{t}} - (\underline{\nabla}\,\underline{u})\cdot\langle\,\rangle - \langle\,\rangle\cdot(\underline{\nabla}\,\underline{u})^{\mathrm{T}}. \tag{20}$$

The third terms in Eqs (17) and (18) represent the direct contribution of the RBCs to the stress due to their convection. This term includes the Laplacian of the respective stress, following the formulation proposed by Bhave et al. [30]. Moreover, the fourth terms imply that the elastic contribution to the viscosity is a linear function of the RBC number density.

For the well-posedness of the problem, the governing equations should be accompanied by consistent boundary conditions. In the axial direction of the vessel, we assume that the velocity (Eq. (14)), the viscoelastic stresses (Eqs (17) and (18)), and the number density of the RBCs and rouleaux (Eqs (12) and (13)) are periodic functions:

$$S(z+L, r) = S(z, r), \tag{21}$$

where S stands for $\underline{u}$, $\underline{\underline{\tau}}$, $\underline{\underline{\sigma}}$, N, M, P_{per}.

On the axis of symmetry ($r = 0$), typical conditions of symmetry are assumed:

$$\underline{n}_{\mathrm{c}}\cdot\underline{u} = 0, \tag{22}$$

$$\underline{n}_{\mathrm{c}}\cdot\underline{\underline{\tau}}\cdot\underline{t}_{\mathrm{c}} = 0, \tag{23}$$

$$\underline{n}_{\mathrm{c}}\cdot\underline{\underline{\sigma}}\cdot\underline{t}_{\mathrm{c}} = 0, \tag{24}$$

$$\underline{n}_{\mathrm{c}}\cdot\underline{J} = 0, \tag{25}$$

$$\underline{n}_{\mathrm{c}}\cdot\underline{I} = 0, \tag{26}$$

where $\underline{n}_{\mathrm{c}}$ is the normal vector and $\underline{t}_{\mathrm{c}}$ the tangent vector to the axis of symmetry.

The vessel wall is assumed to be impermeable and the molecules of the plasma cannot slip along it:

$$\underline{u} = \underline{0}. \tag{27}$$

The red blood cell (RBC) deformability, resulted from their fluid drop-like nature, is partially responsible for the shear-thinning behavior of blood at high RBC concentrations, Chien et al. [41], which also depends on the rouleaux formation and the local hematocrit. The current model for the non-homogeneous blood flow is not based on a detailed description of the deformability and the rotation of RBC membrane as none of the macroscopic or microscopic constitutive models can do this. Such studies, typically examine one (we have performed such a study some time ago, Lac et al. [42]) or rarely, a few RBCs, not the flow overall. However, it accounts explicitly for the effect of membrane elasticity, implicitly for the shear thinning of the blood viscosity (Eq. (A.4) and Eq. (17)) and the alignment of RBCs along the boundary in the direction of the flow by imposing Kramers' equation [43]:

$$\underline{\underline{\tau}} = \frac{1-\beta}{De} N Q_{\mathrm{o}}^2 \underline{t}_{\mathrm{w}} \underline{t}_{\mathrm{w}} - \frac{1-\beta}{De} N \underline{\underline{I}}, \tag{28}$$

where $\underline{t}_{\mathrm{w}}$ is the tangent vector on the wall, and Q_{o} is a scaled dumbbell length (Moyers-Gonzalez et al. [21]). This boundary condition is required because of the inclusion of the term $\nabla^2 \underline{\underline{\tau}}$ in Eq. (17), unlike the models employed by Beris and Mavrantzas [29] and Tsouka et al. [44].

There is no mass flux of the RBCs across the wall:

$$\underline{n}_{\mathrm{w}} \cdot \underline{J} = 0, \tag{29}$$

$$\underline{n}_{\mathrm{w}} \cdot \underline{I} = 0. \tag{30}$$

Finally, we should apply the constraints that the average number density of RBCs in the vessel and the average velocity across the entrance are equal to unity, because they have been scaled with the average number density of RBCs and the average velocity, respectively:

$$\frac{\int\int N r \, \mathrm{d}r \, \mathrm{d}z}{\int\int r \, \mathrm{d}r \, \mathrm{d}z} = 1, \tag{31}$$

$$\iint u_z r \, \mathrm{d}r = 1/2. \tag{32}$$

No such constraint is applied on the rouleaux.

In summary, the mass and momentum balances (Eqs (14) and (15)) directly couple the $\underline{u}$, P and $\underline{\underline{\tau}}$ fields. The latter is determined by the constitutive law (Eq. (17)), which is coupled with the velocity field and the concentration of the RBCs, N, which is determined by Eq. (12). The local viscosity arises in all these equations and is affected by the shear rate, the aggregation–disaggregation kinetics and the concentrations N and M. The concentration of the rouleaux is determined by their population balance (Eq. (13)), which includes the stress they induce and this, in turn, is determined by the constitutive law (Eq. (18)). Therefore, all these equations are intimately interconnected.

3. Numerical scheme

In order to solve numerically the above set of equations we have chosen the mixed finite element method to discretize the velocity, pressure, concentration and stress fields, combined with an elliptic grid generation scheme for the tessellation of the deformed physical domain.

3.1. Elliptic grid generation

First, the domain occupied by the fluid is discretized by a boundary-fitted grid. This is generated by solving a system of quasi-elliptic partial differential equations (see Dimakopoulos and Tsamopoulos [45]). With this scheme the physical domain (r, z) is mapped onto a computational one (η, ζ), which is a cylinder of the same length, but without a constriction. A uniform mesh is generated in the latter domain while, through the mapping, the corresponding mesh in the physical domain follows its deformations. In order to solve the quasi-elliptic partial differential equations, appropriate boundary conditions must be imposed. On the fixed boundaries, we impose the equations that define their position, and the remaining degrees of freedom are used for optimally distributing the nodes along these boundaries with the assistance of the penalty method.

3.2. EVSS formulation

We use the elastic–viscous split stress (EVSS) formulation introduced by Rajagopalan et al. [46] which splits the extra stress tensor into a viscous and a purely elastic part:

$$\underline{\underline{\tau}} = \underline{\underline{T}} + 2(1-\beta)\underline{\underline{\dot{\gamma}}}, \tag{33}$$

$$\underline{\underline{\sigma}} = \underline{\underline{\Sigma}} + 2(1-\beta)\underline{\underline{\dot{\gamma}}}, \tag{34}$$

significantly improving numerical stability even at moderately high *De* numbers.

The success of this scheme resides on the fact that the elliptic nature of the momentum equations is ensured even for $\beta = 0$. Brown et al. [47] proposed a modification of this idea, called EVSS-G, according to which an independent (continuous) interpolation, $\underline{\underline{G}}$, of the components of the velocity gradient tensor, which is discontinuous, if calculated from the velocity finite element interpolation, $\underline{\nabla u}$, is introduced wherever the latter arises in the constitutive equation. Thus compatibility is achieved in the finite element representation between elastic stress, $\underline{\underline{\Sigma}}$, $\underline{\underline{T}}$ and $\underline{\underline{G}}$ in the constitutive equations, even where the velocity vector reduces to zero. This is particularly important for the terms involving spatial derivatives of $\underline{\nabla u}$, which are substituted with derivatives of $\underline{\underline{G}}$. The additional equation that has to be solved is:

$$\underline{\underline{G}} = \underline{\nabla u}. \tag{35}$$

The reformulated constitutive equations of the non-homogeneous model (Eqs (17)–(18)) become:

$$\begin{aligned}
&\underline{\underline{T}} + De\mu(D,N,M)\underline{\underline{\dot{T}}}_{(1)} + 2De\mu(D,N,M)(1-\beta)\underline{\underline{D}}_{(1)} \\
&\quad - \frac{De}{Pe}\mu(D,N,M)\left(\nabla^2\underline{\underline{T}} + (\underline{\underline{\nabla\nabla}} : \underline{\underline{T}})\underline{\underline{I}}\right) - 2\frac{De}{Pe}\mu(D,N,M)(1-\beta)\left(\nabla^2\underline{\underline{D}} + (\underline{\underline{\nabla\nabla}} : \underline{\underline{D}})\underline{\underline{I}}\right) \\
&\quad + 2(1-\beta)(1-N)\underline{\underline{D}} = 0,
\end{aligned} \tag{36}$$

$$\underline{\underline{\Sigma}} + De\mu(D, N, M)\underline{\underline{\dot{\Sigma}}}_{(1)} + 2De\mu(D, N, M)(1-\beta)\underline{\underline{D}}_{(1)} - \frac{De}{Pe}\mu(D, N, M)\big(\nabla^2\underline{\underline{\Sigma}} + (\underline{\underline{\nabla\nabla}} : \underline{\underline{\Sigma}})\underline{\underline{I}}\big) - 2\frac{De}{Pe}\mu(D, N, M)(1-\beta)\big(\nabla^2\underline{\underline{D}} + (\underline{\underline{\nabla\nabla}} : \underline{\underline{D}})\underline{\underline{I}}\big) + 2(1-\beta)(1-M)\underline{\underline{D}} = 0. \tag{37}$$

Finally, applying the EVSS-G transformation in the momentum balance (14) we get:

$$Re\underline{u} \cdot \underline{\nabla u} + \underline{\nabla} P_{\text{per}} + K^2\underline{e}_z - \underline{\nabla} \cdot \underline{\underline{T}} - 2\underline{\nabla} \cdot \underline{\underline{D}} = 0, \tag{38}$$

$$\text{where } \underline{\underline{D}} = \frac{1}{2}\big(\underline{\underline{G}} + \underline{\underline{G}}^{\mathrm{T}}\big). \tag{39}$$

Moreover, the upper convected time derivative becomes:

$$\langle\,\rangle_{(1)} = \frac{D\langle\,\rangle}{Dt} - \langle\,\rangle \cdot \underline{\underline{G}} - \langle\,\rangle \cdot \underline{\underline{G}}^{\mathrm{T}}. \tag{40}$$

3.3. Mixed finite element method

We approximate the velocity, the concentration (in terms of number density) and the position vector with 6-node Lagrangian basis functions, ϕ^i, and the pressure, the elastic stresses, and the velocity gradients with 3-node Lagrangian basis functions, ψ^i. We employ the finite element/Galerkin method, which after applying the divergence theorem results in the following weak forms of the population balances for RBCs and rouleaux becomes:

$$\int_\Omega \big[-\underline{\hat{J}} \cdot \underline{\nabla}\phi^i\big]\,\mathrm{d}\Omega + \int_S [\underline{\hat{J}} \cdot \underline{n}]\phi^i\,\mathrm{d}S = 0, \tag{41}$$

$$\int_\Omega \left[-\underline{\hat{I}} \cdot \underline{\nabla}\phi^i - \frac{\alpha(\dot{\gamma})}{2}M^2 + \frac{b(\dot{\gamma})}{2}(N-M)\right]\mathrm{d}\Omega + \int_S [\underline{\hat{I}} \cdot \underline{n}]\phi^i\,\mathrm{d}S = 0, \tag{42}$$

where $\underline{\hat{J}} = \underline{J} + N\underline{u}$ and $\underline{\hat{I}} = \underline{I} + M\underline{u}$ are the corresponding total mass fluxes, and $\mathrm{d}\Omega$ and $\mathrm{d}\Gamma$ are the differential volume and surface area, respectively. These are the conservative forms of the equations, which are essential for enhancing the stability of the Galerkin formulation at high values of the Peclet number.

The weak forms of Eqs (14) and (15) are given by the following relations:

$$\int_\Omega \big[Re\underline{u} \cdot \underline{\nabla u}\phi^i - P\underline{\nabla}\phi^i - K^2\underline{e}_z\phi^i + \underline{\nabla}\phi^i \cdot \underline{\underline{T}} + 2\underline{\nabla}\phi^i \cdot \underline{\underline{\dot{\gamma}}}\big]\,\mathrm{d}\Omega - \int_S [\underline{n} \cdot \underline{\underline{\tau}}]\phi^i\,\mathrm{d}S = 0, \tag{43}$$

$$\int_\Omega \psi^i \nabla \cdot u\,\mathrm{d}\Omega = 0. \tag{44}$$

The surface integral that appears in the momentum equation is split into four parts, each one corresponding to a boundary of the physical domain (entrance, microvessel-surface, exit and axis boundaries), and the relevant boundary condition is applied.

The continuous approximation of the components of the velocity gradient tensor is determined by:

$$\int_{\Omega} (\underline{\underline{G}} - \underline{\nabla u})\psi^i \, \mathrm{d}\Omega = 0. \tag{45}$$

The strongly convective character of the constitutive equations for the viscoelastic part of the stresses necessitates the use of the SUPG method proposed by Brooks and Hughes [48]. Once more, the adoption of the divergence theorem is necessary due to the second-order terms that appear in Eqs (41) and (42) e.g. $\nabla^2 \underline{\underline{T}} + (\underline{\underline{\nabla\nabla}} : \underline{\underline{T}})\underline{\underline{I}}$:

$$\begin{aligned}
&\int_{\Omega} \Big\{ \big[\underline{\underline{T}} + De\mu(D,N,M)\dot{\underline{\underline{T}}}_{(1)} + 2De\mu(D,N,M)(1-\beta)\underline{\underline{D}}_{(1)} + 2(1-\beta)(\underline{\underline{D}} - N\underline{\underline{D}})\big]\chi^i \\
&\quad - \left[-\frac{De}{Pe}\big(\underline{\nabla}\,\underline{\underline{T}} + (\underline{\underline{\nabla}} \cdot \underline{\underline{T}})\underline{\underline{I}}\big) \cdot \underline{\nabla}\big(\mu(D,N,M)\chi^i\big) \right] \\
&\quad - \left[-2\frac{De}{Pe}(1-\beta)\big(\underline{\nabla}\,\underline{\underline{D}} + (\underline{\underline{\nabla}} \cdot \underline{\underline{D}})\underline{\underline{I}}\big) \cdot \underline{\nabla}\big(\mu(D,N,M)\chi^i\big) \right] \Big\} \, \mathrm{d}\Omega \\
&\quad + \int_S \left[-\frac{De}{Pe}\mu(D,N,M)\big(\underline{\nabla}\,\underline{\underline{T}} + (\underline{\underline{\nabla}} \cdot \underline{\underline{T}})\underline{\underline{I}}\big) \cdot \underline{n} \right] \chi^i \, \mathrm{d}S \\
&\quad + \int_S \left[-2\frac{De}{Pe}\mu(D,N,M)(1-\beta)\big(\underline{\nabla}\,\underline{\underline{D}} + (\underline{\underline{\nabla}} \cdot \underline{\underline{D}})\underline{\underline{I}}\big) \cdot \underline{n} \right] \chi^i \, \mathrm{d}S = 0,
\end{aligned} \tag{46}$$

$$\begin{aligned}
&\int_{\Omega} \Big\{ \big[\underline{\underline{\Sigma}} + De\mu(D,N,M)\dot{\underline{\underline{\Sigma}}}_{(1)} + 2De\mu(D,N,M)(1-\beta)\underline{\underline{D}}_{(1)} + 2(1-\beta)(\underline{\underline{D}} - M\underline{\underline{D}})\big]\chi^i \\
&\quad - \left[-\frac{De}{Pe}\big(\underline{\nabla}\,\underline{\underline{\Sigma}} + (\underline{\underline{\nabla}} \cdot \underline{\underline{\Sigma}})\underline{\underline{I}}\big) \cdot \underline{\nabla}\big(\mu(D,N,M)\chi^i\big) \right] \\
&\quad - \left[-2\frac{De}{Pe}(1-\beta)\big(\underline{\nabla}\,\underline{\underline{D}} + (\underline{\underline{\nabla}} \cdot \underline{\underline{D}})\underline{\underline{I}}\big) \cdot \underline{\nabla}\big(\mu(D,N,M)\chi^i\big) \right] \Big\} \, \mathrm{d}\Omega \\
&\quad + \int_S \left[-\frac{De}{Pe}\mu(D,N,M)\big(\underline{\nabla}\,\underline{\underline{\Sigma}} + (\underline{\underline{\nabla}} \cdot \underline{\underline{\Sigma}})\underline{\underline{I}}\big) \cdot \underline{n} \right] \chi^i \, \mathrm{d}S \\
&\quad + \int_S \left[-2\frac{De}{Pe}\mu(D,N,M)(1-\beta)\big(\underline{\nabla}\,\underline{\underline{D}} + (\underline{\underline{\nabla}} \cdot \underline{\underline{D}})\underline{\underline{I}}\big) \cdot \underline{n} \right] \chi^i \, \mathrm{d}S = 0,
\end{aligned} \tag{47}$$

where the weighting function χ^i is formed from the finite element basis function for the elastic stress components according to:

$$\chi^i = \psi^i + \frac{h_{\mathrm{ch}}}{\sqrt{1 + |\underline{u}|^2}}\underline{u} \cdot \underline{\nabla}\psi^i, \tag{48}$$

where $|\underline{u}|$ is the magnitude of the mean velocity and h_{ch} is a characteristic length in each element. The mean velocity $|\underline{u}|$ in an element is defined as $|\underline{u}| = (1/3)\sum_{n=1}^{3} |\underline{u}|_n$, $|\underline{u}|_n$ denoting the magnitude of the velocity at the vertices of the corresponding triangular element. As a characteristic length, h_{ch}, we used the square root of the area of each triangular element.

The entire set of algebraic equations is solved simultaneously for all variables (velocities, pressure, stresses and species concentration). For a mesh of 40,000 triangular elements, the number of unknowns is 808,422. The coordinates of the mesh are recomputed only when the constriction ratio is varied. The Jacobian matrix that results from each iteration is stored in Compressed Sparse Row (CSR) format, and the linearized set of equations is solved using the MUMPS solver, a robust direct sparse matrix solver, Amestoy et al. [49,50]. The iterations of the Newton–Raphson method are terminated using a tolerance for the absolute residual vector set at 10^{-9}. The code was written in Fortran 90 and was run on a workstation with a dual 16-core Opteron AMD CPU and required about two days to compute each steady state.

The code is validated by simulating some of the cases presented in Ref. [21] for blood flow in straight vessels. The results, which are not shown here for conciseness, are in excellent agreement with those calculations [21] within a tolerance of 0.5×10^{-7}. In particular, we have calculated all the physical fields for the physical properties given in Table 1 of Ref. [21] and $\tilde{R}_{\max} = 500$ μm, $\tilde{K} = -10\ \mathrm{Nm}^{-3}$. We have also compared our results graphically and in terms of the Euclidean norm with those shown in Figs 3 and 5 of Ref. [21]. The Euclidean norm of the deviation ($\|\underline{X}_{\mathrm{p}} - \underline{X}_{\mathrm{MG}}\|$) has been defined as the difference between the nodal values of a field (e.g. $\underline{X} = \underline{v}$) calculated via our algorithm ($\underline{X}_{\mathrm{p}}$) and the corresponding one presented in Ref. [21] ($\underline{X}_{\mathrm{MG}}$).

4. Results and discussion

We have performed a parametric analysis on the problem presented above. Typical values of the dimensional scales that we used are given in Table 1 (Moyers-Gonzalez et al. [21] and [51]). In particular, we study three cases of different flow rates through rigid tubes in the size range of small coronary arteries (Table 2), as obtained from Thurston [25], Moyers-Gonzalez et al. [21] and Matsumoto and Kajiya [52]. Case I corresponds to a slow flow, where both Reynolds and Deborah numbers are low, while cases II and III correspond to faster flows where these two dimensionless numbers take moderate values. The flow conditions in cases I and II comes from *in vitro* experiments, but those of case III comes from *in vivo* measurements. For clarity, the relevant dimensionless parameters and numbers are included in Table 2. It should be noted that the selected characteristic velocities for cases I and II correspond to oscillatory blood flow in rigid tubes [10,21], while case III represents a physiological blood flow [52]. In general, the rigid wall boundary conditions considered here make this work more relevant to *in vitro* experiments of blood flow than to physiological flow in human vessels.

The results that will follow will be presented in terms of the number density of RBCs and rouleaux, velocity and stress contours and in terms of the number density, velocity, and pressure drop plots along the entrance, wall and axis of symmetry. We aim to examine how the migration of RBCs affects the flow and stress fields and is affected by them. We also define two interfacial integrals to evaluate the tube haematocrit H_{T} and the discharge haematocrit H_{D} from the local concentration of the RBCs, N, and the axial velocity $u_z(r, z = 0)$ (Damiano et al. [53], Lei et al. [54], Lipowsky et al. [55]):

$$H_{\mathrm{T}} = 2 \int_0^1 N(r, z = 0) r \, \mathrm{d}r, \tag{49}$$

$$H_{\mathrm{D}} = 4 \int_0^1 N(r, z = 0) u_z(r, z = 0) r \, \mathrm{d}r. \tag{50}$$

Table 2
Values of characteristic dimensions and related non-dimensional parameters for blood flow through various rigid tubes

Parameter	Symbol	Case I value	Case II value	Case III value
Vessel radius (m)	$\tilde{R}_{\max}$	4.3×10^{-4}	2.5×10^{-4}	2.0×10^{-4}
Average velocity (m/s)	$\tilde{u}_{\mathrm{m}}$	2.4×10^{-3}	7.0×10^{-2}	0.1
Characteristic time (s)	$\tilde{R}_{\max}/\tilde{u}_{\mathrm{m}}$	0.179	3.571×10^{-3}	2.0×10^{-3}
Characteristic shear rate (s^{-1})	$\tilde{u}_{\mathrm{m}}/\tilde{R}_{\max}$	5.581	280.0	500.0
Dimensionless	$\dot{\gamma}_{\mathrm{cr}}$	1.035	2.062×10^{-2}	1.156×10^{-2}
Dimensionless	$\dot{\gamma}_{\max}$	161.25	3.21	1.80
Dimensionless viscosity	β	0.299	0.299	0.299
Dimensionless	η_0	3.26×10^{-2}	3.26×10^{-2}	3.26×10^{-2}
Dimensionless	η_∞	2.34×10^{-3}	2.34×10^{-3}	2.34×10^{-3}
Dimensionless	θ	1.940	7,929.36	27,166.67
Dimensionless	ε	27.033	110,468.88	378,475.92
Deborah number	De	2.790×10^{-2}	1.40	2.50
Peclet number	Pe	5,160	87,500	100,000
Reynolds number	Re	0.3255	5.520	6.308

Note: Case I is obtained from Thurston [9], case II from Moyers-Gonzalez et al. [21] and case III from Fig. 6 (top) of Matsumoto and Kajiya [52].

4.1. Predictions for slow flows (case I)

Here we present for the first time predictions of the non-homogeneous model in a 2D flow. We begin its evaluation by studying a numerically easier case (case I in Table 2), where the average velocity is low $\tilde{u}_{\mathrm{m}} = 2.4 \times 10^{-3}$ m/s in a narrow vessel $\tilde{R}_{\max} = 4.3 \times 10^{-4}$ m. The corresponding Reynolds number is low, $Re = 0.325$, thus the flow is creeping, the Deborah number is also low, $De = 2.79 \times 10^{-2}$, which means that the RBCs behave as rigid particles, and the Peclet number has a moderate value, $Pe = 5{,}160$, implying that both advection and diffusion mechanisms are significant. Computation of the flow and stress fields is easier because of the low De. In this range of De, convergence of the calculations is not inhibited by the high Weissenberg problem. To study the effect of geometry, we perform a continuation of our numerical solution with respect to the amplitude of the geometric variation (c_{r}), starting from $c_{\mathrm{r}} = 1$ (straight vessel) and gradually decreasing its value while keeping the rest of the dimensionless parameters of the problem constant. Typical numerical results are shown in Figs 2–5 (and Figs 10–12 of Supplementary material), which are discussed below.

By examining the contour plots of the two velocity components u_{r} and u_z in Fig. 2, we draw the conclusion that for the specific set of parameters the velocity field is well developed along the entrance and exit parts of the microvessel. Moreover, the effect of inertia is so low that the radial velocity component is antisymmetric with respect to the plane $z = 5$, even for the lowest values of c_{r}. This velocity component takes negative values along the constricting section of the vessel and positive values along the expanding section, in agreement with the variation of the vessel wall. As c_{r} decreases, both velocity components in the constriction increase drastically. In contrast, the velocity profiles along the entrance are little affected by the change of the wall shape. The variation of the periodic part of the pressure increases by about a factor of 4–5 with each decrease in c_{r} and is always maximized just before the constriction.

Next we will comment on the computed stress components. According to the Moyers-Gonzalez et al. model [21] the total stress is composed of the small, Newtonian-like contribution form the plasma and

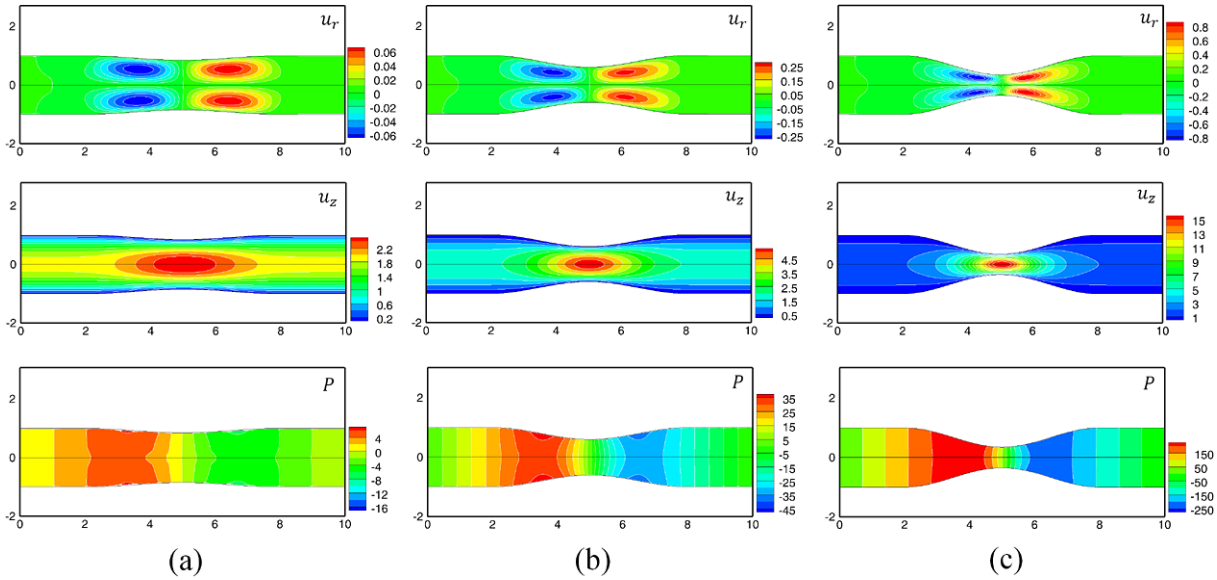

Fig. 2. Contour plots of the u_r and u_z velocity components and P_{per}: (a) $c_r = 0.85$, (b) $c_r = 0.60$ and (c) $c_r = 0.35$ for case I of Table 2. (Colors are visible in the online version of the article; http://dx.doi.org/10.3233/BIR-14033.)

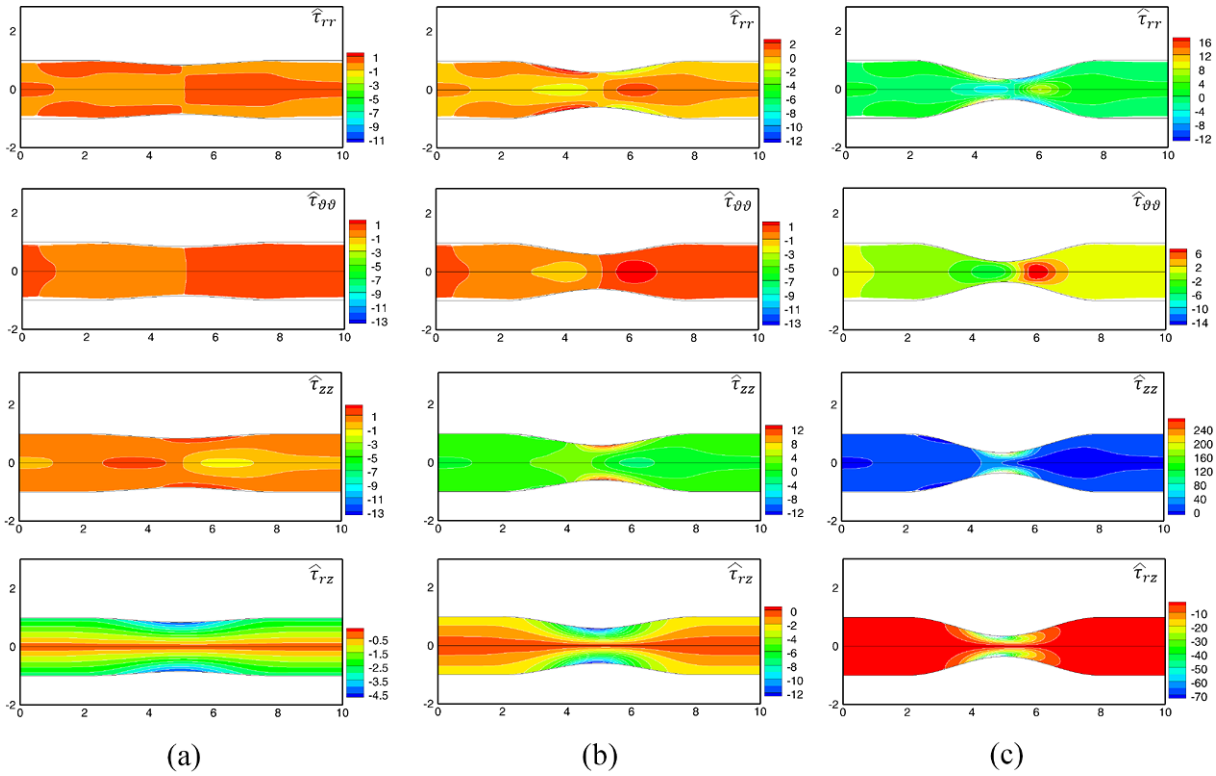

Fig. 3. Contours of the normal components of the total stress tensor $\hat{\tau}_{rr}$, $\hat{\tau}_{\theta\theta}$, $\hat{\tau}_{zz}$ and $\hat{\tau}_{rz}$: (a) $c_r = 0.85$, (b) $c_r = 0.60$ and (c) $c_r = 0.35$ for case I of Table 2. (Colors are visible in the online version of the article; http://dx.doi.org/10.3233/BIR-14033.)

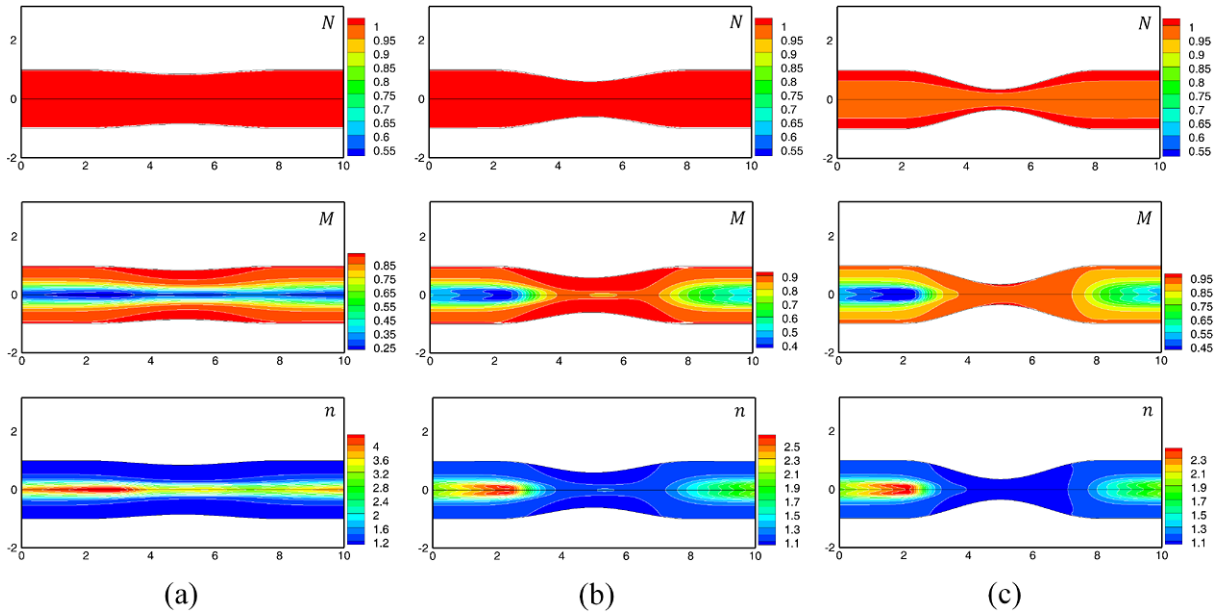

Fig. 4. Contours of N, M and n: (a) $c_r = 0.85$, (b) $c_r = 0.60$ and (c) $c_r = 0.35$ for case I of Table 2. (Colors are visible in the online version of the article; http://dx.doi.org/10.3233/BIR-14033.)

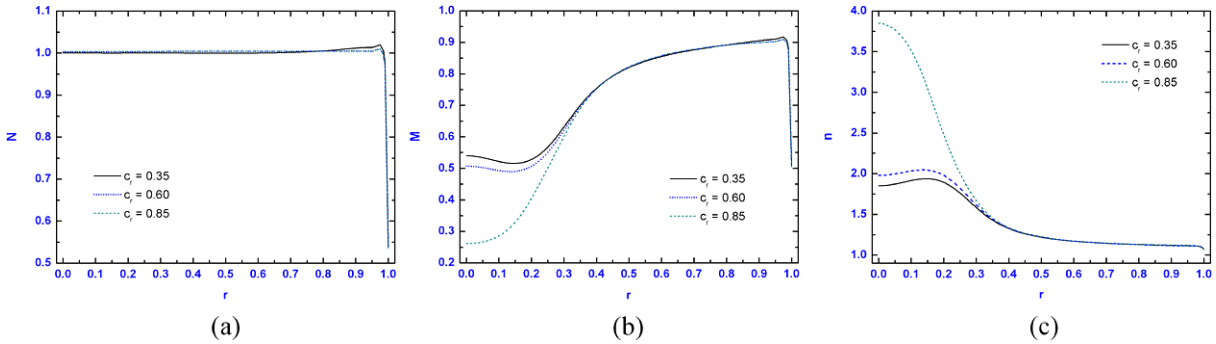

Fig. 5. Profiles of N, M and n along the entrance: (a) $c_r = 0.85$, (b) $c_r = 0.60$ and (c) $c_r = 0.35$ for case I of Table 2. (Colors are visible in the online version of the article; http://dx.doi.org/10.3233/BIR-14033.)

the elastic-like contribution from the single red blood cells:

$$\hat{\underline{\underline{\tau}}} = \underline{\underline{\tau}} + \beta\left(\nabla \underline{u} + \nabla \underline{u}^{\mathrm{T}}\right). \tag{51}$$

Regarding the normal stress components (Fig. 3) for $c_r = 0.85$ and 0.60, they all vary almost in the same range, but in more constricted vessels, $c_r = 0.35$, the prominent role of $\hat{\tau}_{zz}$ becomes apparent. In terms of numbers, its maximum value is more than an order of magnitude larger than the other two normal stress components. Moreover, we observe the development of very sharp boundary layers along the constricted part of the vessel wall in all stress components. Similarly, the variation of the total shear stress increases as c_r decreases and is always dominant around the constriction. Details from the distribution of $\hat{\tau}_{rr}$, $\hat{\tau}_{zz}$ and $\hat{\tau}_{rz}$ and the corresponding components of the rate of strain tensor along

the wall are depicted in Fig. 10 of the Supplementary material. The stress components exhibit a wavy variation, which is different from the corresponding component of the rate of strain tensor. The range of their variation is significantly smaller, about 2 or 3 orders of magnitude, because the migration of the RBCs towards the core region of the vessel, reduces the effective viscosity and, hence, the stress components only. The total shear stress takes very small values that increase as c_{r} decreases (Fig. 10, Supplementary material). The wall shear stress in the straight part of the vessel could not be compared to physiological blood flow, as the characteristic vessel radius and maximum blood velocity correspond to oscillatory flow in rigid tubes (Thurston [10]). On the other hand, the $\dot{\gamma}_{rr}$ and $\dot{\gamma}_{zz}$ components are zero away from the constriction, exhibit a wavy variation which goes along with an exchange of the sign before and after the constriction and have opposite to each other signs around the minimum of the cell radius. The shear rate $\dot{\gamma}_{rz}$ is negative and is minimized at the constriction (Fig. 10, Supplementary material). Comparing numerical predictions for the exerted shear stress to the measurements of Thurston [10], $\hat{\tau}_{rz}$ is underestimated suggesting that the model of Moyers-Gonzalez et al. [21] cannot fully capture blood's viscoelasticity. This can be attributed to limitations of the model related to the stress boundary conditions as well as to the model's assumptions for the lack of dependence of the diffusivity on the hematocrit, and the hindered effects of walls.

Some very important information that only the non-homogeneous model can offer is shown in Figs 4 and 5. In the first row of Fig. 4, the dimensionless number density (normalized concentration) of the RBCs is shown for $c_{\mathrm{r}} = 0.85, 0.60$ and 0.35. Irrespective of the value of c_r, the number density (N) in the bulk is a little bit higher than unity, but there is a very thin region along the wall that the concentration is less than unity. In other words, a concentration boundary layer appears along it. From Fig. 5(a) where the distribution of the RBC concentration is shown, we can see that the thickness of the boundary layer is almost 0.025 and N at the wall is about 0.54. Thus, there is a migration of the RBCs to the core which, as already mentioned, is responsible for the reduction of the stresses there. N retains this value along the straight part of the wall, but it increases somewhat along the constriction (Fig. 11(a) of the Supplementary material). The maximum value of N along the wall is located at the middle ($z = 5$) and it is followed by a local minimum ($z = 6.5$), in order for the constraint Eq. (31) to be satisfied. The maximum value increases as c_{r} decreases, due to the reduction of the cross-section of the vessel and increased deformation of the RBCs. Indicatively, for $c_{\mathrm{r}} = 0.3$, the maximum value is $N = 0.6375$; 17.5% higher than the maximum value of N for $c_{\mathrm{r}} = 0.6$. Along the axis of symmetry (Fig. 12(a) of the Supplementary material), the number density of RBCs is almost constant, exhibiting only very small variations around the constriction.

The relaxation time and the viscosity of blood strongly depend on the concentration of rouleaux M and the size of rouleaux n (see Appendix A.2). It should be mentioned that rouleaux size equal to unity means that there are only individual cells. Typically we expect that rouleaux will develop in regions where the rate of deformation is low. In the second and the third rows of Fig. 4, the contour plots of M and n are depicted. Near the entrance, the RBCs form rouleaux of average size $n = 2$–3.5 and hence reducing the local rouleaux number density M, due to the low absolute value of shear stress. In other words, there is a small number of RBCs that form pairs and triplets. Near the constriction, the absolute value of shear stress increases significantly, breaking up the rouleaux, increasing their number density, but reducing their average size. Details of the variations of M and n are shown in Fig. 5, as well as in Figs 11 and 12 of the Supplementary material. Along the entrance (Fig. 5(c)) and for all values of c_{r}, the average size is almost equal to unity away from the centreline. For smaller radial distances, there is a deviation among the curves of n, which increases as c_{r} increases. The number density of rouleaux (Fig. 5(b)) is an increasing function of the radial distance up to 0.95. There, a sharp boundary layer

develops, which is similar to the boundary layer in N. The average size of rouleaux along the wall is almost constant and equal to unity (Fig. 11(c), Supplementary material). Thus, the number density of rouleaux M (Fig. 11(b), Supplementary material) coincides with N (Fig. 11(a), Supplementary material). Regarding the distribution of RBCs and rouleaux along the axis of symmetry (Fig. 12, Supplementary material), the latter exhibits significantly larger variations due to the effect of the geometry on the rate of deformation of the blood in the core region (Fig. 4). It should be mentioned that the rate of deformation of the blood controls the rate of aggregation and disaggregation of RBCs via Eqs (A.1) and (A.2). Thus the average rouleaux size is high when the constriction is low (Fig. 12(c), Supplementary material), or close to unity when c_r has moderate values.

4.2. *Predictions for faster flows (case II)*

Another case that we have extensively studied is case II of Table 2, based on the study of Moyers-Gonzalez et al. [21]. The maximum radius of the vessel is almost two times smaller (2.5×10^{-4} m) compared to the previous case I, but the average velocity is about 30 times higher, 7.0×10^{-2} m/s. Consequently, the effect of inertia on the flow ($Re = 5.52$) as well as on the convective transfer of RBCs ($Pe = 87{,}500$) will be higher. Moreover, the effect of viscoelasticity will be more pronounced ($De = 1.40$). All these factors make the corresponding calculations more difficult and the continuation procedure fails in small values of c_r.

The high value of inertia has a pronounced influence on the velocity fields (Fig. 6). The radial velocity field is no longer antisymmetric across the plane $z = 5$. Its isolines are convected downstream, and their convection gets more intense as c_r decreases. Regarding the axial velocity u_z, the point where it is maximized is not located at the midpoint of the axis of symmetry, but is shifted downstream in the expanding region of the microvessel. From closer examination of Fig. 6, we conclude that the length of the vessel for the current flow conditions is not so long for a fully developed flow to arise, and this affects somewhat the velocity profiles in the entrance and the exit.

Both the normal and shear stresses are affected by the higher convection (Fig. 7 and Figs 13, 14 in Supplementary material). In comparison with the distribution of stresses in Figs 3 and 4, the boundary

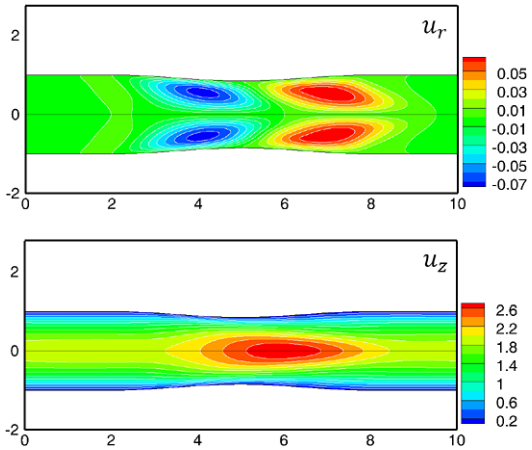

Fig. 6. Contour plots of the u_r and u_z velocity components: $c_r = 0.85$, for case II of Table 2. (Colors are visible in the online version of the article; http://dx.doi.org/10.3233/BIR-14033.)

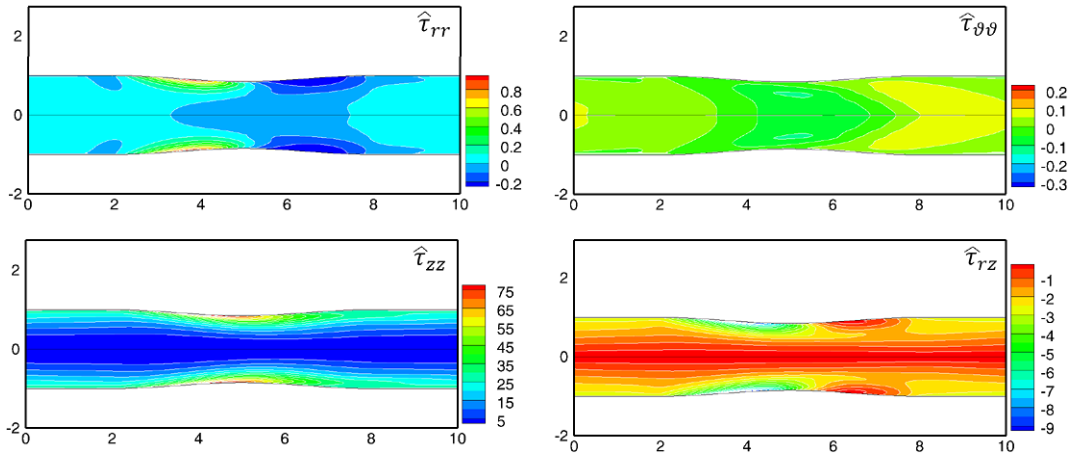

Fig. 7. Contours of the normal components of the total stress tensor $\hat{\tau}_{rr}$, $\hat{\tau}_{\theta\theta}$, $\hat{\tau}_{zz}$ and $\hat{\tau}_{rz}$: $c_r = 0.85$ for case II of Table 2. (Colors are visible in the online version of the article; http://dx.doi.org/10.3233/BIR-14033.)

layers are sharper and the variation of the stresses is larger. The dominant stress component is always $\hat{\tau}_{zz}$ (Fig. 7) due to the large effect of viscoelasticity in the main flow direction. Indicatively, the maximum value of $\hat{\tau}_{zz}$ for $c_r = 0.85$ is higher than 75 (Fig. 7). The corresponding values of $\hat{\tau}_{rr}$ and $\hat{\tau}_{\theta\theta}$ are one to two orders of magnitude smaller, while the shear stress assumes negative values, which in absolute value are about 5–6 times smaller than the axial normal stress. Regarding the magnitude of the rate of strain, it is comparable with $\hat{\tau}_{rz}$ and consequently significantly smaller than $\hat{\tau}_{zz}$. The magnitude of the shear stress takes its minimum value at the wall, because of the migration of RBCs away from the wall (Fig. 14, Supplementary material). Actually along the wall the shear stress is almost zero. However, its magnitude increases sharply just away from the wall and before the constriction because of the vessel geometry. After the constriction and near the wall remains as small as around the center line. Moreover, the variations along the wall of each one of $\dot{\gamma}_{rr}$, and $\dot{\gamma}_{zz}$ for $c_r = 0.85$ are almost antisymmetric (Fig. 14, Supplementary material), but for smaller c_r this antisymmetry breaks.

If we examine the distribution of the number density of RBCs N (Fig. 8), we realize that it exhibits larger variations along a cross section. In contrast to case I (Fig. 4), the profiles of N do not vary monotonically (as they did in case I), due to stronger convection. Moreover, along the axis of symmetry the average rouleaux size slightly exceeds 5, but the rouleaux concentration M is lower than 0.2. Thus, a few rouleaux of longer sizes (n) are formed. Along the vessel wall, the concentrations of both N and M are almost constant. For smaller values of c_r, the variations are larger. Along the axis of symmetry, the concentration variations are smaller in comparison to those on the wall.

4.3. Global characteristics (cases I–III)

By examining the effect of c_r on the macroscopic pressure drop, K^2, between the entrance and exit boundaries of the vessel (Fig. 9(a)), we conclude that K^2 decreases monotonically with c_r and in exactly the same way for cases I, II and III. From additional numerical tests we found that K^2 is slightly affected by De, Pe, and the rest of the model parameters except for Re. All curves follow closely the master one of Fig. 9(a) which is governed by the geometric characteristics of the vessel. In the absence of stress gradient induced phenomena, the variation of both K^2 and wall drag coefficient should be very similar. However, the migration of RBCs away from the wall, along with the development of stress and

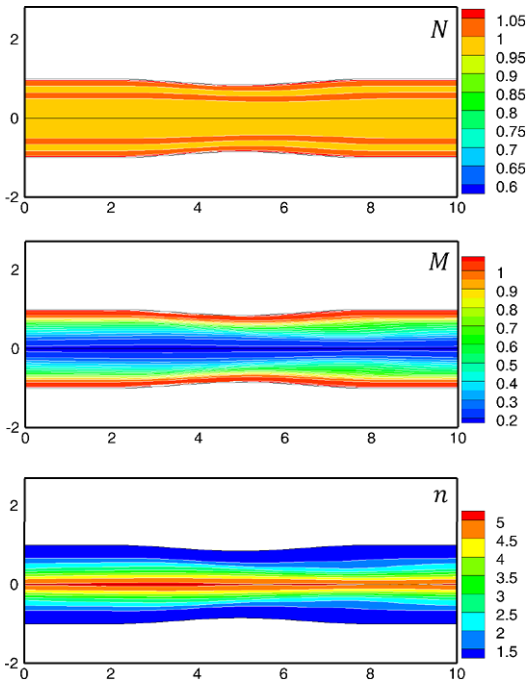

Fig. 8. Contours of N, M and n: $c_r = 0.85$ for case II of Table 2. (Colors are visible in the online version of the article; http://dx.doi.org/10.3233/BIR-14033.)

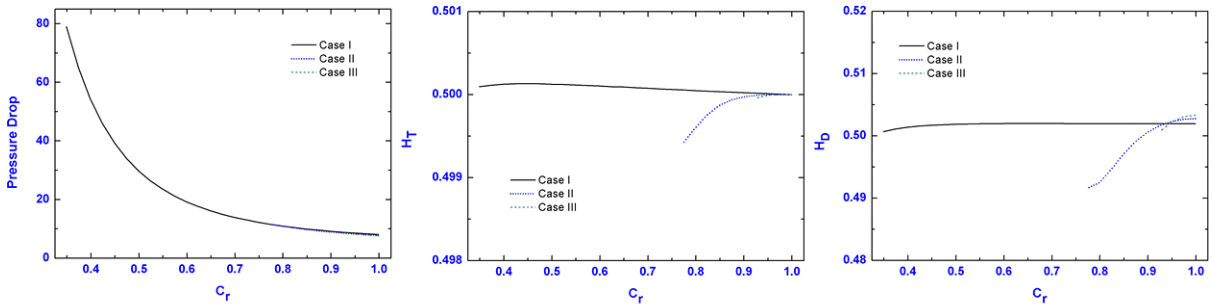

Fig. 9. Variation of: (a) the Pressure Drop, (b) H_T and (c) H_D along the entrance as a function of c_r. For cases I–III. (Colors are visible in the online version of the article; http://dx.doi.org/10.3233/BIR-14033.)

population boundary layers, decreases the wall drag force as a function of c_r, and eventually it tends to zero. An exception of this rule is again case I, which corresponds to the widest vessel. In this case migration phenomena seem to play a less significant role compared to the effect of inertia on the plasma stresses. This should have been expected given the fact that in case I the radius of the vessel is the largest.

In Fig. 9(b) and (c), the tube and discharge haematocrit and the corresponding quantities for the number density of rouleaux defined in Eqs (49) and (50) are presented for all the cases of Table 2. From $c_r = 1.0$ to $c_r \approx 0.90$, the variation of H_T and H_D (Fig. 9(b) and (c)) is very small, but below this point the curves diverge significantly. More specifically, for the case I, H_T and H_D are identical and

almost equal to the imposed value 0.5 (Eq. (31)), while the other two cases seem to be slightly affected by the reduction of the constriction ratio c_r. Apparently, the corresponding discharge haematocrit H_D is significantly lower than H_T. Case III, which has the largest effect of viscoelasticity, presents the steepest reduction with decreasing c_r.

5. Conclusions

We have studied the flow of blood in a stenotic vessel using the rheological model of Moyers-Gonzalez et al. [21], which accounts for RBC migration due to gradients of the stress tensor in the fluid. The flow is driven by a macroscopic pressure gradient and all fields are periodic in the z-direction. The blood has constant mass density and viscosity proportional to the chain number density. The governing equations describing the transport phenomena relevant for such a flow are those corresponding to an inhomogeneous model whose three components (the plasma, the individual RBCs and the rouleaux) are assumed to be in thermal but not in hydrodynamic equilibrium.

We have solved this complex set of coupled equations under steady state conditions using the mixed finite element method. Simulations up to fairly high Deborah numbers, wide range of Peclet numbers and pronounced channel constrictions have been successfully carried out by using the EVSS-G method for the computation of the elastic stresses, the SUPG method for the weighting of the constitutive equations, and a pseudo-elliptic method to generate a boundary-conforming mesh.

We have calculated the distribution of RBCs and the rouleaux in vessels of varying diameter under slow and fast flows as reported *in vitro* and *in vivo* experiments, respectively. The results show that a cell-depleted layer develops along the vessel wall with an almost constant thickness for slow flow conditions. Viscoelastic effects in blood flow were found to be responsible for steeper decreases of tube and discharge hematocrits as decreasing function of constriction ratio. This causes the reduction of the drag force as the constriction ratio decreases. The drag force also depends moderately on the dimensionless parameters of the problem. On the other hand, the macroscopic pressure gradient seems to be significantly less sensitive to the problem parameters for slow flows, and an increasing function of the reduction of the constriction ratio. Comparison of the calculated shear stresses to experimental measurements suggests that the model cannot accurately account for the effect of the elastic stresses in blood flow. The effect of anisotropic hindered diffusion due to wall effects and the hydrodynamic interaction between the RBCs should be incorporated in the model, in order its overall accuracy to be improved.

Acknowledgements

This work has been supported financially by the Research Promotion Foundation (RPF) of the Republic of Cyprus under the program "DESMI 2009–2010" (Grant number: 3411-2106, title: Accelerating FSI solvers using general purpose graphical processing units (GPGPUs) – FSISOVERS ΤΠΕ/ΠΛΗΡΟ/0609(ΒΕ)/11) of the framework programme "For research, technological development and innovation 2009–2010" co-funded by the Republic of Cyprus and European Regional Development Fund.

Appendix

A.1. Nomenclature

Symbol	Units	Description
$\tilde{N}$	$1/m^3$	Number density of RBCs
$\tilde{M}$	$1/m^3$	Number density of Rouleau
n	–	Average rouleau size
n_{st}	–	Average rouleaux size in steady state
$\tilde{k}_B$	$m^2kg \cdot s^{-2}K^{-1}$	Boltzmann constant
$\tilde{D}_{tr}$	m^2/s	Coefficient of translational diffusivity
$\tilde{T}$	K	Temperature
$\tilde{\kappa}$	$m^2kg \cdot s^{-2}$	Impacts with the other RBCs constant
$\underline{\underline{\tilde{\tau}}}$	N/m^2	Total elastic stress tensor
$\tilde{\rho}_f$	kg/m^3	Constant mass density of blood
$\tilde{P}$	N/m^2	Pressure
$\underline{\underline{\tilde{\dot{\gamma}}}}$	s^{-1}	Rate of strain tensor
$\tilde{\dot{\gamma}}_{cr}$	s^{-1}	Critical rate of strain
$\tilde{\dot{\gamma}}_{max}$	s^{-1}	Maximum rate of strain
$\tilde{u}_{av}$	m/s	Average velocity
$\tilde{\eta}_{st}$	kg/ms	Steady RBCs viscosity
$\tilde{\eta}_p$	kg/ms	Plasma viscosity
$\tilde{\eta}_c$	kg/ms	RBCs viscosity
$\tilde{\eta}_t$	kg/ms	Total viscosity
$\tilde{\eta}_0$	kg/ms	Zero-shear rate viscosity
$\tilde{\eta}_\infty$	kg/ms	High-shear rate viscosity
$\tilde{\mu}(\tilde{\dot{\gamma}})$	s	Relaxation time function
$\underline{\underline{I}}$	–	unit tensor
$\tilde{\alpha}(\tilde{\dot{\gamma}})$	s^{-1}	Aggregation rate of RBCs
$\tilde{b}(\tilde{\dot{\gamma}})$	s^{-1}	Disaggregation rate of RBCs

A.2. Kinetic equations for RBC aggregation

Motivated from the work of Murata and Secomb [56] and Shiga et al. [57] the dimensionless aggregation rate $a(\dot{\gamma})$ for fixed dynamic haematocrit equal to the feed haematocrit is defined as:

$$a(\dot{\gamma}) = \begin{cases} \sum_{i=0}^{3} \alpha_{1,i} \dot{\gamma}^i, & \dot{\gamma} \leqslant \dot{\gamma}_{crit}, \\ \sum_{i=0}^{3} \alpha_{2,i} \dot{\gamma}^i, & \dot{\gamma}_{crit} \leqslant \dot{\gamma} \leqslant \dot{\gamma}_{max}, \\ 0, & \dot{\gamma} \geqslant \dot{\gamma}_{max}, \end{cases} \tag{A.1}$$

where:

$$\alpha_{1,0} = 1, \qquad \alpha_{1,2} = \frac{3\alpha_{1,0}}{\dot{\gamma}_{\text{crit}}^2}, \qquad \alpha_{1,3} = \frac{-2\alpha_{1,0}}{\dot{\gamma}_{\text{crit}}^3},$$

$$\alpha_{2,0} = \frac{2\alpha_{1,0}\dot{\gamma}_{\text{max}}^2(-\dot{\gamma}_{\text{max}} + 3\dot{\gamma}_{\text{crit}})}{-\dot{\gamma}_{\text{max}}^3 - 3\dot{\gamma}_{\text{max}}\dot{\gamma}_{\text{crit}}^2 + \dot{\gamma}_{\text{crit}}^3 + 3\dot{\gamma}_{\text{crit}}\dot{\gamma}_{\text{max}}^2},$$

$$\alpha_{2,1} = \frac{-12\dot{\gamma}_{\text{crit}}\alpha_{1,0}\dot{\gamma}_{\text{max}}}{-\dot{\gamma}_{\text{max}}^3 - 3\dot{\gamma}_{\text{max}}\dot{\gamma}_{\text{crit}}^2 + \dot{\gamma}_{\text{crit}}^3 + 3\dot{\gamma}_{\text{crit}}\dot{\gamma}_{\text{max}}^2},$$

$$\alpha_{2,2} = \frac{6\alpha_{1,0}(\dot{\gamma}_{\text{max}} + \dot{\gamma}_{\text{crit}})}{-\dot{\gamma}_{\text{max}}^3 - 3\dot{\gamma}_{\text{max}}\dot{\gamma}_{\text{crit}}^2 + \dot{\gamma}_{\text{crit}}^3 + 3\dot{\gamma}_{\text{crit}}\dot{\gamma}_{\text{max}}^2},$$

$$\alpha_{2,3} = \frac{-4\alpha_{1,0}}{-\dot{\gamma}_{\text{max}}^3 - 3\dot{\gamma}_{\text{max}}\dot{\gamma}_{\text{crit}}^2 + \dot{\gamma}_{\text{crit}}^3 + 3\dot{\gamma}_{\text{crit}}\dot{\gamma}_{\text{max}}^2},$$

where the dimensional critical shear rate is chosen as $\tilde{\dot{\gamma}}_{\text{crit}} = 5.78\ \text{s}^{-1}$ and the maximum shear rate $\tilde{\dot{\gamma}}_{\text{max}} = 900\ \text{s}^{-1}$. The dimensionless fragmentation rate $b(\dot{\gamma})$ is determined from $a(\dot{\gamma})$ that holds in steady flow:

$$b(\dot{\gamma}) = \frac{a(\dot{\gamma})}{n_{\text{st}}(n_{\text{st}} - 1)}, \tag{A.2}$$

where n_{st} is the steady average rouleaux size defined as:

$$n_{\text{st}} = \frac{\eta_0}{\eta_\infty}\left(\frac{1 + \theta\dot{\gamma}^{\text{m}}}{1 + \varepsilon\dot{\gamma}^{\text{m}}}\right)\left(1 + \frac{3}{2}De \cdot \alpha(\dot{\gamma})\right), \tag{A.3}$$

where η_0 and η_∞ are the zero- and the infinite-shear-rate RBCs viscosities both scaled with η_{t} and the $\eta_{\text{st}}(\dot{\gamma})$ is the dimensionless steady RBCs viscosity given from the Cross model:

$$\eta_{\text{st}}(\dot{\gamma}) = \eta_0\left(\frac{1 + \theta\dot{\gamma}^{\text{m}}}{1 + \varepsilon\dot{\gamma}^{\text{m}}}\right), \tag{A.4}$$

where θ, ε, m are the Cross model parameters (Table 1).

The actual relaxation time of the rouleaux is smaller than the sum of the single Maxwell relaxation times of the red blood cells due to the supplementary relaxation mechanism involved in the fragmentation process. Thus, the dimensionless relaxation time of the rouleaux $\mu(\dot{\gamma}, n)$ is defined:

$$\mu(\dot{\gamma}, N, M) = \frac{N/M}{1 + Deg(\dot{\gamma}, N, M)(N/M)}, \tag{A.5}$$

where g is the disaggregation coefficient given by the equation:

$$g(\dot{\gamma}, N, M) = 0.5b(\dot{\gamma})(N/M - 1) + a(\dot{\gamma})M. \tag{A.6}$$

References

[1] Popel AS, Johnson PC. Microcirculation and hemorheology. Annu Rev Fluid Mech. 2005;37:43–69.
[2] Lipowsky HH. Microvascular rheology and hemodynamics. Microcirculation. 2005;12:5–15.
[3] Freund JB. Numerical simulation of flowing blood cells. Annu Rev Fluid Mech. 2014;46:67–95.
[4] Sharan M, Popel AS. A two-phase model for flow of blood in narrow tubes with increased effective viscosity near the wall. Biorheology. 2001;38:415–28.
[5] Baskurt OK. Handbook of hemorheology and hemodynamics. Amsterdam, The Netherlands: IOS Press; 2007.
[6] Chien S. Biophysical behavior of red blood cells in suspension. In: Surgenor DM, editor. The red blood cell, Vol. II. New York: Academic Press; 1975. p. 1031–133.
[7] Chien S, Usami S, Taylor HM, Lundberg JL, Gregersen MI. Effects of hematocrit and plasma proteins on human blood rheology at low shear rates. J Appl Physiol. 1966;21:81–7.
[8] Meiselman H. Red blood cell aggregation: 45 years being curious. Biorheology. 2009;46:1–19.
[9] Thurston GB. Frequency and shear rate dependence of viscoelasticity of human blood. Biorheology. 1973;10:375–81.
[10] Thurston GB. Elastic effects in pulsatile blood flow. Microvasc Res. 1975;9:145–57.
[11] Evans EA, Hochmuth RM. Membrane viscoelasticity. Biophysical J. 1976;16(1):1–11.
[12] Apostolidis A, Beris A. Modeling of the blood rheology in steady-state shear flows. J Rheol. 2014;58:607–33. doi:10.1122/1.4866296.
[13] Quemada D. A non-linear Maxwell model of biofluids: Application to normal human blood. Biorheology. 1993;30:253–65.
[14] Williams MC, Rosenblatt JS, Soane DS. Theory of blood rheology based on a statistical mechanics treatment of rouleaux, and comparisons with data. Int J Polym Mater. 1993;21:57–63.
[15] Vlastos G, Lerche D, Koch B. The superposition of steady on oscillatory shear and its effect on the viscoelasticity of human blood and a blood-like model fluid. Biorheology. 1997;34:19–36.
[16] Dimakopoulos Y, Bogaerds A, Anderson P, Hulsen M, Baaijens FPT. Direct numerical simulation of a 2D idealized aortic heart valve at physiological flow rates. Comp Meth Biomech and Biomed Engrg. 2012;15(11):1157–79.
[17] Anand M, Rajagopal KR. A shear-thinning viscoelastic fluid model for describing the flow of blood. Int J of Cardiovascular Medicine and Science. 2004;4(2):59–68.
[18] Rajagopal KR, Srinivasa AR. A thermodynamic frame work for rate type fluid models. J Non-Newtonian Fluid Mech. 2000;80:207–27.
[19] Bodnar T, Sequeira A. Numerical study of the significance of the non-Newtonian nature of blood in steady flow through a stenosed vessel. In: Rannacher R, Sequeira A, editors. Advances in mathematical fluid mechanics. Springer; 2010. p. 83–104.
[20] Chakraborty D, Bajajb M, Yeob L, Friendb J, Pasquali M, Prakash JR. Viscoelastic flow in a two-dimensional collapsible channel. J Non-Newtonian Fluid Mech. 2010;165:1204–18.
[21] Moyers-Gonzalez MA, Owens RG, Fang J. A non-homogeneous constitutive model for human blood. Part I. Model derivation and steady flow. J Fluid Mech. 2008;617:327–54.
[22] Owens RG. A new microstructure-based constitutive model for human blood. J Non-Newtonian Fluid Mech. 2006;140:57–70.
[23] Bureau M, Healy JC, Bourgoin D, Joly M. Rheological hysteresis of blood at low shear rate. Biorheology. 1980;17:191–203.
[24] Fang J, Owens RG. Numerical simulations of pulsatile blood flow using a new constitutive model. Biorheology. 2006;43:637–60.
[25] Thurston GB. Rheological parameters for the viscosity, viscoelasticity and thixotropy of blood. Biorheology. 1979;16:149–62.
[26] Iolov A, Kane AS, Bourgault Y, Owens RG, Fortin A. A FEM for a microstructure-based model of blood. Intern J Numerical Meth in Biomedical Eng. 2011;27(9):1321–49.
[27] Fahraeus R. The suspension stability of the blood. Physiol Rev. 1929;9:241–79.
[28] Fahraeus R, Lindqvist T. The viscosity of blood in narrow capillary tubes. Am J Physiol. 1931;96:562–8.
[29] Beris AN, Mavrantzas VG. On the compatibility between various macroscopic formalisms for the concentration and flow of dilute polymer solutions. J Rheol. 1994;38:1235–50.
[30] Bhave AV, Armstrong RC, Brown RA. Kinetic theory and rheology of dilute, nonhomogeneous polymer solutions. J Chem Phys. 1991;95:2988–3000.
[31] Cook LP, Rossi LF. Slippage and migration in models of dilute wormlike micellar solutions and polymeric fluids. J Non-Newtonian Fluid Mech. 2004;116(2,3):347–69.
[32] Rossi LF, McKinley G, Cook LP. Slippage and migration in Taylor–Couette flow of a model for dilute wormlike micellar solutions. J Non-Newtonian Fluid Mech. 2006;136:79–92.

[33] Pries AR, Neuhaus D, Gaehtgens P. Blood viscosity in tube flow: Dependence on diameter and hematocrit. Am J Physiol Heart Circ Physiol. 1992;263:H1770–H1778.
[34] Sutera SP, Seshadri V, Croce PA, Hochmuth RM. Capillary blood flow: II. Deformable model cells in tube flow. Microvasc Res. 1970;2:420–33.
[35] Caro CG, Pedley TJ, Schroter RC. Atheroma and arterial wall shear: Observation, correlation and proposal of shear dependent mass transfer mechanism for atherogenesis. Proc Roy Soc London B. 1971;177:109–59.
[36] Zydney AL, Colton CK. Augmented solute transport in the shear-flow of a concentrated suspension. PCH PhysicoChem Hydrodynamics. 1988;10:77–96.
[37] Bishop JJ, Popel AS, Intaglietta M, Johnson PC. Effect of aggregation and shear rate on the dispersion of red blood cells flowing in venules. Am J Physiol Heart Circ Physiol. 2002;283(5):H1985–H1996.
[38] Acrivos A. Shear-induced particle diffusion in concentrated suspensions of noncolloidal particles. J Rheol. 1995;39:813–26.
[39] Pranay P, Henriquez-Rivera RG, Graham MD. Depletion layer formation in suspensions of elastic capsules in Newtonian and viscoelastic fluids. Phys Fluids. 2012;2(4):061902.
[40] Ma H, Graham MD. Theory of shear-induced migration in dilute polymer solutions near solid boundaries. Phys Fluids. 2005;17:083103.
[41] Chien S, Usami S, Dellenback RJ, Gregersen MI. Shear-dependent deformation of erythrocytes in rheology of human blood. Am J Physiol. 1970;219:136–42.
[42] Lac E, Pelekasis N, Barthes-Biesel D, Tsamopoulos J. Spherical capsules in three-dimensional unbounded Stokes flows: Effect of the membrane constitutive law and onset of buckling. J Fluid Mech. 2004;516:303–34.
[43] Kramers HA. Het gedrag van macromoleculen in een stroomende vloeistof. Physica. 1944;11:1–19.
[44] Tsouka S, Dimakopoulos Y, Mavrantzas V, Tsamopoulos J. Stress-gradient induced migration of polymers in corrugated channels. J Rheol. 2014;58(4):911–47.
[45] Dimakopoulos Y, Tsamopoulos J. A quasi-elliptic transformation for moving boundary problems with large anisotropic deformations. J Computational Phys. 2003;192:494–522.
[46] Rajagopalan D, Armstrong RC, Brown RA. Finite element methods for calculation of steady, viscoelastic flow using constitutive equations with a Newtonian viscosity. J Non-Newtonian Fluid Mech. 1990;36:159–92.
[47] Brown RA, Szady MJ, Northey PJ, Armstrong RC. On the numerical stability of mixed finite-element methods for viscoelastic flows governed by differential constitutive equations. Theoretical Comp Fluid Dynamics. 1993;5:77–106.
[48] Brooks AN, Hughes TJR. Streamline upwind/Petrov–Galerkin formulations for convection dominated flows with particular emphasis on the incompressible Navier–Stokes equations. Comp Methods Applied Mech Eng. 1982;32:199–259.
[49] Amestoy PR, Duff IS, Koster J, L'Excellent J-Y. A fully asynchronous multifrontal solver using distributed dynamic scheduling. SIAM J Matrix Anal Applic. 2001;23(1):15–41.
[50] Amestoy PR, Guermouche A, L'Excellent J-Y, Pralet S. Hybrid scheduling for the parallel solution of linear systems. Paral Comp. 2006;32(2):136–56.
[51] Moyers-Gonzalez MA, Owens RG, Fang J. A non-homogeneous constitutive model for human blood. Part III. Oscillatory flow. J Non-Newtonian Fluid Mech. 2008;155:161–73.
[52] Matsumoto T, Kajiya F. Coronary microcirculation: Physiology and mechanics. Fluid Dynamics Research. 2005;37:60–81.
[53] Damiano ER, Long DS, Smith ML. Estimation of viscosity profiles using velocimetry data from parallel flows of linearly viscous fluids: Application to microvascular haemodynamics. J Fluid Mech. 2004;512:1–19.
[54] Lei H, Fedosov DA, Caswell B, Karniadakis GE. Blood flow in small tubes: Quantifying the transition to the non-continuum regime. J Fluid Mech. 2013;722:214–39.
[55] Lipowsky HH, Usami S, Chien S. In vivo measurements of "apparent viscosity" and microvessel hematocrit in the mesentery of the cat. Microvasc Res. 1980;19:297–319.
[56] Murata T, Secomb TW. Effects of shear rate on rouleaux formation in simple shear flow. Biorheology. 1988;25:113–22.
[57] Shiga T, Imaizumi K, Harada N, Sekiya M. Kinetics of rouleaux formation using TV image analyzer. I. Human erythrocytes. Am J Physiol. 1983;245:H252–H258.

Supplementary material

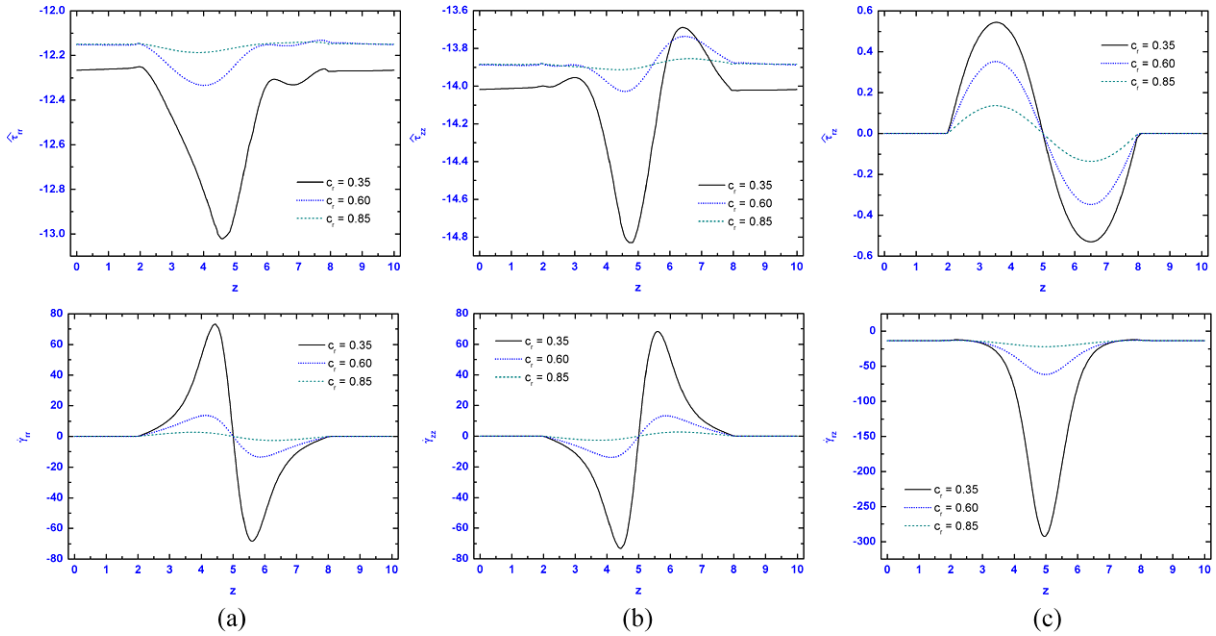

Fig. 10. Plots of $\hat{\tau}_{rr}$, $\hat{\tau}_{zz}$, $\hat{\tau}_{rz}$ and $\dot{\gamma}_{rr}$, $\dot{\gamma}_{zz}$, $\dot{\gamma}_{rz}$ along the vessel wall: (a) $c_{\mathrm{r}} = 0.85$, (b) $c_{\mathrm{r}} = 0.60$ and (c) $c_{\mathrm{r}} = 0.35$ for case I of Table 2. (Colors are visible in the online version of the article; http://dx.doi.org/10.3233/BIR-14033.)

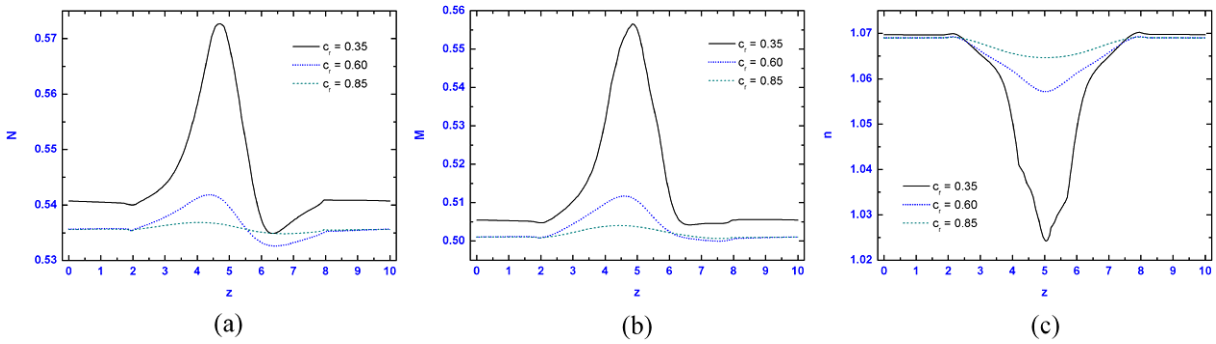

Fig. 11. Plots of N, M and n along the vessel wall: (a) $c_{\mathrm{r}} = 0.85$, (b) $c_{\mathrm{r}} = 0.60$ and (c) $c_{\mathrm{r}} = 0.35$ for case I of Table 2. (Colors are visible in the online version of the article; http://dx.doi.org/10.3233/BIR-14033.)

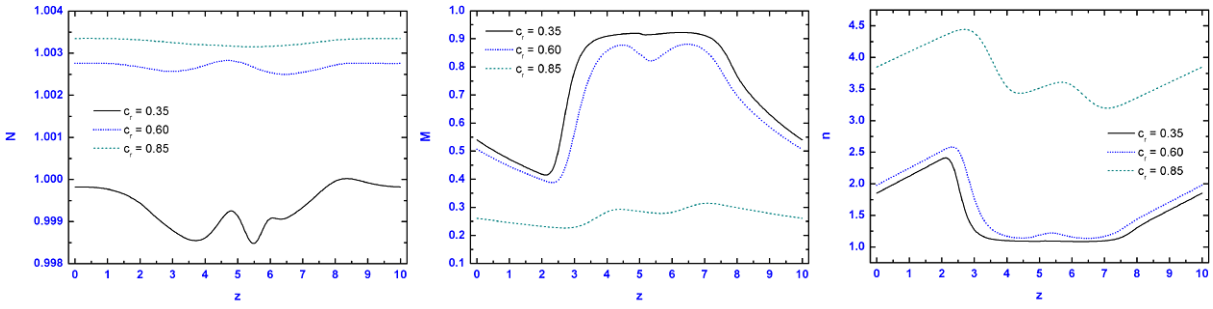

Fig. 12. Plots of N, M and n along the axis of symmetry: (a) $c_{\mathrm{r}} = 0.85$, (b) $c_{\mathrm{r}} = 0.60$ and (c) $c_{\mathrm{r}} = 0.35$ for case I of Table 2. (Colors are visible in the online version of the article; http://dx.doi.org/10.3233/BIR-14033.)

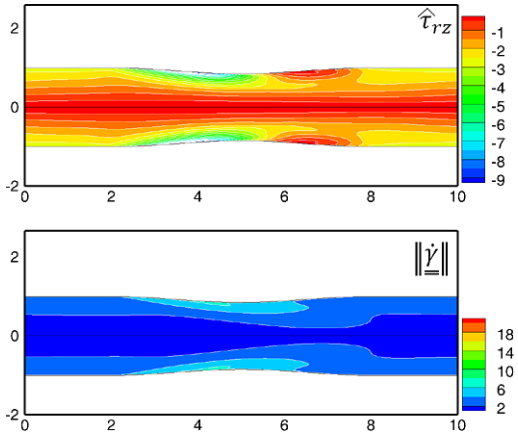

Fig. 13. Contours of $\hat{\tau}_{rz}$ and $\|\dot{\gamma}\|$: $c_{\mathrm{r}} = 0.85$ for case II of Table 2. (Colors are visible in the online version of the article; http://dx.doi.org/10.3233/BIR-14033.)

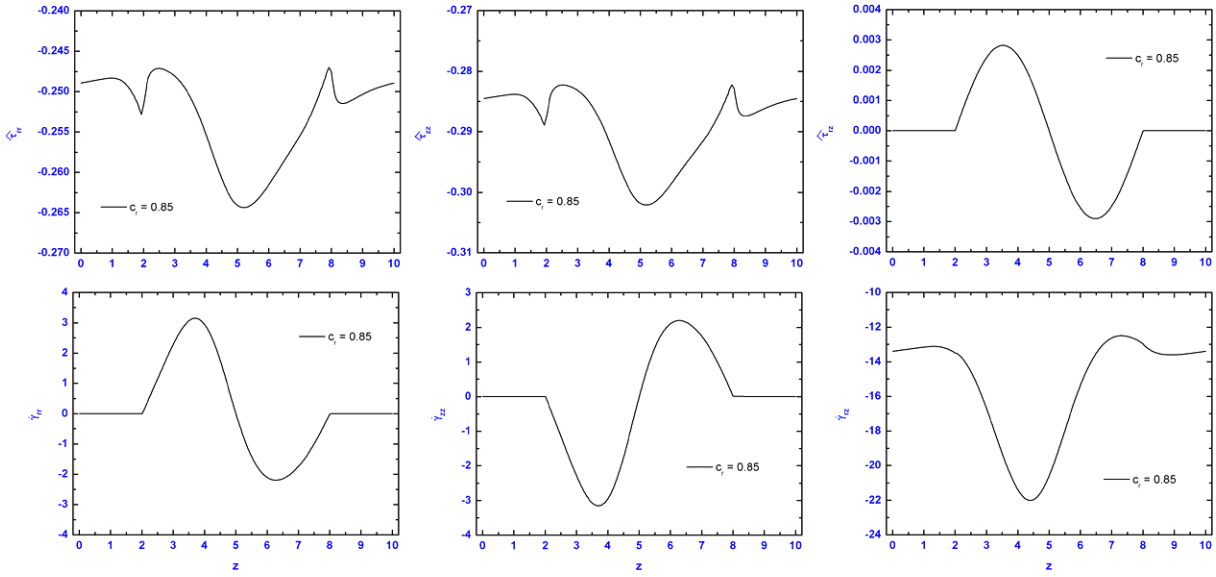

Fig. 14. Plots of $\hat{\tau}_{rr}$, $\hat{\tau}_{zz}$, $\hat{\tau}_{rz}$ and $\dot{\gamma}_{rr}$, $\dot{\gamma}_{zz}$, $\dot{\gamma}_{rz}$ along the vessel wall: (a) $c_{\mathrm{r}} = 0.85$ and (b) $c_{\mathrm{r}} = 0.60$ for case II of Table 2. (Colors are visible in the online version of the article; http://dx.doi.org/10.3233/BIR-14033.)